Probabilistic axial capacity model for concrete-filled steel tubes accounting for load eccentricity and debonding

Alessandro Contento[a], Angelo Aloisio[b,*], Junqing Xue[c], Giuseppe Quaranta[a], Bruno Briseghella[c], Paolo Gardoni[d]

[a] Department of Structural and Geotechnical Engineering, Sapienza University of Rome, Rome, Italy.
[b] Department of Civil, Construction-Architecture and Environmental Engineering, University of L'Aquila, L'Aquila, Italy.
[c] College of Civil Engineering, Fuzhou University, Fuzhou, China.
[d] Department of Civil and Environmental Engineering, University of Illinois at Urbana-Champaign, Urbana, Illinois, USA.

Abstract

Concrete-filled steel tubular (CFST) columns are increasingly used around the world because they offer two significant advantages. The first one is the composite action of the steel tube and infilled concrete, which enhances the strength and ductility of the columns. The second one is the use of the steel tube as a permanent formwork for concrete casting, which allows saving construction time and costs. Although considerable research and several experimental tests have been carried out on CFST columns, there is not a probabilistic model for the evaluation of their axial capacity yet. Additionally, the effects of the axial load eccentricity and debonding have received little attention so far. Within this framework, the present paper proposes a physics-based probabilistic model to predict the ultimate axial capacity of CFST columns, which is developed as the sum of a deterministic part and a probabilistic correction term, together with two additional corrective models to describe its reduction due to load eccentricity and debonding, which are developed coherently with the axial capacity model as probabilistic correction terms. The accuracy of the proposed models is compared with that of existing capacity equations already in use within technical standards and available literature. Additionally, this study provides uncertainty factors to allow using the proposed capacity model for design applications. Thanks to their very good accuracy and compact form, the proposed models are suitable to be included within technical standards. On the other hand, differently from common deterministic models, they can also be updated as new experimental data are available.

Keywords: Axial capacity; Concrete-filled steel tube; Debonding; Load eccentricity; Probabilistic capacity model; Uncertainty factors.

1. Introduction

Concrete-filled steel tubular (CFST) columns are largely employed around the world owing to the fact that they offer two significant advantages. The first one is the composite action of the steel tube and infilled concrete, which enhances the strength and ductility of the columns. The steel tube effectively confines the concrete core, thereby providing a highly ductile response under compression and increasing the overall energy dissipation capacity [1]. The second advantage is the use of the steel tube as a permanent formwork for concrete casting, which helps to reduce construction time and costs. The combination of good structural performances and limited costs makes these structural elements attractive for the design of several structures and infrastructures (particularly arch bridge ribs and bridge piers [2–5]).

Since the first tests by Klöppel and Goder [6], several researchers carried out laboratory experiments to assess the structural performance of CFST columns [7–12]. The large amount of information resulting from such experimental tests was collected by Thai et al. [13] in order to create a comprehensive database for CFST columns. The experimental evidences show that the structural performance of CFST columns largely depends on the confinement effect provided by the steel tube on the concrete core. In fact, an improved structural performance can be achieved if the confinement exerted by the steel tube persists at higher strains ranges of both concrete and steel. Thus, the combined use of high-strength concrete and steel can further increase the axial capacity of CFST columns. For this reason, some experimental tests on CFST columns also aimed at determining the performance of CFST columns made of high-strength materials [14–38]. However, the use of high-strength materials may significantly reduce the economic advantage provided by CFST columns.

Although considerable research and several experimental tests have been carried out to assess the response of CFST columns under axial compression [39–46], there is still a need

*Corresponding author.
Email address: angelo.aloisio1@univaq.it (Angelo Aloisio)

for accurate and reliable capacity equations that also benefit from the availability of larger and more detailed datasets. Additionally, the effects of the eccentricity of the applied axial load and that of the debonding phenomenon – which can significantly jeopardize the axial capacity of CFST columns – have received little attention so far. This lack of investigations mirrors in the axial capacity equations for CFST columns included into current technical standards, which are not in good agreement with the experimental data as demonstrated in [7]. As an example, the formulation provided by the Eurocode 4 (EC4) may lead up to a 17% error in the prediction of the ultimate capacity [47]. Moreover, with the exception of the Chinese design codes [48, 49], existing technical standards lack formulations that include the effect of debonding in the prediction of the axial capacity of CFST columns.

Recently, some researches proposed accurate data-driven models for the axial capacity of CFST columns by means of supervised learning algorithms [50–57]. However, such models are not supported by a mechanics-based understanding like those included into current technical standards. For example, although in some cases the initial regressors are based on the understanding of the underlying physical phenomena, the functional forms of the explanatory functions (i.e., the regression terms) and the models usually contain higher-order terms that are selected only because they are statistically significant and consequently lack physical meanings. Therefore, the main limitation of these recent data-driven approaches is the lack of consistency with the derivation of the existing code provisions. Moreover, regardless their accuracy level, all cited models are deterministic and not suitable for reliability analyses. Consequently, there is a need for accurate physics-based probabilistic models of the axial capacity for CFST columns that include the effects of load eccentricity and debonding, in such a way to allow their use within current technical standards.

Within this framework, the present paper proposes a physics-based probabilistic model to predict the axial capacity of CFST columns with circular cross-section, together with two additional corrective models to describe the detrimental effects due to load eccentricity and debonding. Such models are derived by means of the general procedure reported in [58]. Ultimately, they identify the most influential parameters affecting the mechanical behaviour of CFST columns under compression and, at the same time, account for the prevailing uncertainties. Probabilistic models can be either data-driven or physics-based.

Both the data-driven and the proposed physics-based models are calibrated with data and as such fall in the same broader category of empirical models. However, considering the three fundamental steps in developing a probabilistic model 1) selection of regressors/explanatory functions, 2) calibration of the model parameters, and 3) interpretation of the results, data-driven models (e.g., [59]) and physics-based models (e.g., [58]) differ in the first and/or third step. Data-driven models exclusively, or at least largely, rely on the empirical evidence provided by the data to select the explanatory functions. Therefore, if statistically significant, every combination of the initial regressor is accepted in the final model form. Additionally, in most cases, for data-driven models the physical acceptability of the resulting model form is not considered. On the contrary, for physics-based models, the understanding of the physics of the problem is the basis not only in the choice of the regressors but also in the development of the explanatory functions that are constructed based on the physical phenomena.

The model for the axial capacity of CFST columns is formulated by adding suitable correction terms to the plastic axial capacity (i.e., the sum of the concrete and steel plastic capacity). Such correction terms include explanatory functions (which are based on the physics of the relevant phenomena) and unknown model parameters calibrated through a Bayesian approach by means of the experimental data previously used in [13]. The reduction of the ultimate capacity due to axial load eccentricity and debonding is modeled via correction factors that represent the ratio between the axial capacity of the CFST column without imperfections under centered compression and the corresponding values with load eccentricity or debonding, respectively. The models of such correction factors include explanatory functions similar to those used for the model of the axial capacity and additional specific explanatory functions that accounts for the characteristics of the axial load eccentricity and debonding. The unknown model parameters for debonding factor (i.e., the correction factor for debonding) and eccentricity factor (i.e., the correction factor for the eccentricity of the applied axial load) are calibrated by means of the datasets employed in [60] and [13], respectively, which both contain experimental data already analysed in the literature.

The accuracy of the proposed models is compared with that of existing capacity equations already in use into technical standards and existing literature. In order to allow the implementation of the proposed models into current technical standards, uncertainty factors are also derived. Although the present study is meant at estimating the axial capacity of CFST columns in which the debonding factor refers to circumferential debonding only, the proposed methodology has a general validity and can be used to obtain physics-based probabilistic models for the flexural and shear capacity of CFST columns taking into possible account circular-gap debonding. The very good accuracy and the compact form make the proposed models suitable to be included within technical standards. Because of the data-driven calibration, the validity of the proposed models is restricted by the range of available experimental data. Differently from available deterministic models, however, the proposed probabilistic approach copes with such issue to some extent, since it allows for the effective models updating as new experimental data are available.

Following this Introduction, Section 2 describes the mechanics behind the axial capacity of CFST columns. Then, Section 3 presents both the formulation of the proposed models and the methodology used for model selection and calibration. Next, Section 4 introduces the experimental data and the calibrated models. Finally, Section 5 presents the derivation of the uncertainty factors.

2. Response of CFST columns under axial compression

2.1. Axial capacity of CFST columns

In the last decades, multiple experimental findings [47, 61–63] proved that the axial capacity of CFST columns N_u is generally higher than the sum of the axial capacities of their components, which are the steel tube and the concrete core. This mechanical behaviour is represented by the following inequality:

$$N_u - (f_c A_c + f_y A_s) > 0, \tag{1}$$

where f_c is the concrete compressive strength, f_y is the steel yielding strength whereas A_c and A_s are the cross-sectional areas of concrete and steel, respectively. This behavior is attributable to the confinement effect provided by the steel tube on the concrete core. This confinement effect, originally highlighted in [64], determines an increment of the compressive strength of the concrete [65] that varies during the loading process of the

CFST columns.

The loading process of the CFST columns can be divided into three phases [66–70]. In the initial loading phase, the confinement effect can be neglected, since the Poisson coefficient of the concrete ν_c is smaller than the Poisson coefficient of the steel ν_s. Therefore, in the radial direction, the steel tube expands faster than the concrete core that does not benefit from any confinement effect. In this initial phase, the steel tube is subjected to compressive stresses, with no separation between the tube itself and the concrete core. In the intermediate phase, the applied load reaches the level of the uni-axial strength of the concrete, and concrete micro-cracking increases. The lateral expansion of the concrete reaches its maximum and mobilizes the steel tube that, in turn, now confines efficiently the concrete core. In this phase, the concrete core is subjected to a triaxial stress state, while the steel tube is in a biaxial stress state. In the last phase, the steel tube reaches the maximum confinement capacity, and the concrete core collapses with the steel tube. Examples of the failure mechanisms that characterize this last phase are presented in [71].

According to this mechanical behaviour, N_u can be estimated as the sum of the axial capacities of steel tube and confined concrete core by means of specific correction factors as follows:

$$N_u \simeq (f_{cc}A_c + \alpha_s f_y A_s)\,, \tag{2}$$

where α_s is the factor that accounts for the reduction of the axial capacity due to the presence of the biaxial stress state inside the steel tube, and f_{cc} is the compressive strength of the confined concrete.

Following Barlow's formula [72], it is assumed that the maximum tensile stress in the steel tube equals the steel yielding strength. Therefore, the axial capacity of CFST columns can be written as follows:

$$N_u \simeq \left\{1 + \left[\alpha_c k_c \left(\frac{2t}{D}\right)\frac{f_y}{f_c}\right]\right\} f_c A_c + \alpha_s f_y A_s. \tag{3}$$

where α_c is a scale factor for the concrete core [73, 74], k_c is a confinement coefficient [75, 76], t and D are the thickness and outer diameter of the CFST column. In a more compact form, Eq. (3) can be rewritten as follows:

$$N_u \simeq f_c A_c \left(1 + \alpha_c k_c \psi + \alpha_a \xi\right), \tag{4}$$

where $\psi = (2t/D)/(f_y/f_c)$ and $\xi = f_y A_s / f_c A_c$. In technical standards [77] and the literature [47, 78], Eq. (3) is often presented as

$$N_u \simeq \alpha'_c f_c A_c + \alpha_a f_y A_s, \tag{5}$$

assuming a constant value for α'_c, which accounts for both scale and confinement effects separately expressed by α_c and k_d in Eq. (3).

The values of α_s, α_c, k_c, and α'_c vary among the available formulations. Some examples are reported in Appendix, which provide a summary of some formulations for N_u reported into technical standards [77, 79] and recent studies [47, 78].

2.2. Effects of load eccentricity and debonding on the axial capacity of CFST columns

Both load eccentricity and debonding cause a reduction of the axial capacity of CFST columns. The eccentricity of the applied axial load generates a bending moment on the CFST column. In a generic cross-section, the tangential stresses combine with the normal stresses and lead to the collapse of the column for a value of N_u lower than expected. Some technical standards (e.g., [79]) and papers (e.g., [80]) provide formulations that account for the combined effect of axial force and bending moment on CFST columns, but the analysis of such load combination is out of the scopes of this paper because they involve failure mechanisms different from those relevant for the present study and would require the development of specific capacity models. However, for small values of the load eccentricity (e.g., eccentricity due to construction tolerances), it is common expedient to estimate the reduced axial capacity of CFST columns N_{ue} as a fraction of N_u,

$$N_{ue} = k_e N_u, \tag{6}$$

in which k_e is a reduction factor depending on the eccentricity of the applied axial load e as well as on the geometric and constitutive characteristics of the CFST columns $\mathbf{s}$, i.e.,

$k_e = k_e(e, \mathbf{s})$.

Debonding is the loss of adhesion between steel tube and concrete core due to the presence of initial imperfections or defects, and manifests itself as gaps between the two materials. Such a loss of adhesion prevents the transmission of contact forces and reduces the confinement effect of the steel tube on the concrete core. Several researchers attempted to assess the reduction of the axial capacity of CFST columns due to debonding from experimental tests [71, 81–87]. Xue et al. [60] used the results of such experimental tests to develop models for the axial capacity of CFST columns and debonding factor (i.e., the ratio between the axial capacity of CFST columns with and without debonding). Although such nonlinear regression models based on the Evolutionary Polynomial Regression technique exhibit a satisfactory agreement with the experimental data, they have no mechanical basis. Despite the existing experimental studies, there is still a significant lack of knowledge on the origin of debonding (such as the imperfections of the concrete core or steel tube) as well as the need for models to quantify the consequent reduction of the axial capacity of CFST columns.

Also in the case of debonding, it is common expedient to estimate the reduced axial capacity of CFST columns N_{ud} as a fraction of N_u,

$$N_{ud} = k_d N_u. \tag{7}$$

In this case, k_d is a reduction factor depending on the geometric characteristics of the debonding $\mathbf{d}$ as well as on the geometric and constitutive characteristics of the CFST columns $\mathbf{s}$, i.e., $k_d = k_d(\mathbf{d}, \mathbf{s})$.

There are two typologies of debonding related to the shape of the steel-concrete gap, namely the circular-segment and the circumferential debonding gap. The circular-segment (or spherical-cap) gap derives from poor construction quality and difficulties in concrete pouring [71] as in curved CFST, where the core is usually filled by pumping concrete. The process of pumping concrete into the hollow tube can generate a circular-segment gap at the top of the concrete section. The circular-segment gap is described by the de-fill rate, which is the ratio between the debonding and concrete areas. The circumferential gap depends on debonding forces originated by the different deformation of concrete core and steel tube, generally caused by concrete shrinkage or thermal gradients. This type of debonding can be described by three parameters that are the debonding thickness T_d, the radial extension of the debonding ψ_d described by the arclength ratio $R_d = \psi_d/2\pi$, and the debonding length L_d.

In both cases, the effect of debonding occurs in the intermediate phase of the loading process of the CFST columns. In most cases, the debonding thickness is less than 3 mm [49, 88]. As the concrete core micro-cracking starts, it expands and reaches the steel tubes. The presence of the initial gap between the steel tube and the concrete core is associated with a higher micro-cracking of concrete before the concrete core reaches the inner surface of the steel tube. Therefore, such higher micro-cracking results in a lower capacity of the concrete core to generate a higher confining pressure. Additionally, the presence of asymmetric debonding determines a higher steel stresses where there is no gap. The asymmetry of the stress state inside the steel tubes may cause a further reduction of the steel resistance.

3. Probabilistic models for the axial capacity of CFST columns

The initial part of this Section (i.e., Subsections 3.1-3.3) presents the theory behind the formulation and calibration of the proposed models. The second part of the Section (i.e., Subsections 3.4-3.6) illustrates the models proposed in the paper and the set of explanatory functions used for each of them.

3.1. Probabilistic model formulation

Following [58], the proposed form of the axial capacity and reduction factors is written as follows:

$$T\left[C\left(\mathbf{x},\boldsymbol{\Theta}\right)\right] = T\left[\hat{C}\left(\mathbf{x}\right)\right] + \gamma\left(\mathbf{x},\boldsymbol{\theta}\right) + \sigma\varepsilon, \tag{8}$$

where $T(\cdot)$ is a variance stabilizing transformation, $C(\mathbf{x},\boldsymbol{\Theta})$ is the dimensionless capacity, $\mathbf{x}$ are the measurable capacity variables, and $\boldsymbol{\Theta} = \{\boldsymbol{\theta},\sigma\}$ are unknown model parameters. On the right side of Eq. (8), $\hat{C}\left(\mathbf{x}\right)$ is a deterministic model based on mechanics rules (also borrowed directly from technical standards), $\gamma\left(\mathbf{x},\boldsymbol{\theta}\right)$ is a correction term based on mechanics rules and evidence derived from the experimental data. The product $\sigma\varepsilon$ is the model error, with model standard deviation σ and normally distributed random variable

ε. The model is based on three assumptions: additivity (i.e., the additivity of $\sigma\varepsilon$); homoskedasticity (i.e., the independence of σ from $\mathbf{x}$); normality (i.e., the normality of ε). Through a suitable choice of $T(\cdot)$, such assumptions can be approximately satisfied in the transformed space, within the range of the data used to calibrate the model.

The correction term $\gamma(\mathbf{x}, \boldsymbol{\theta})$ is selected as a linear combination of n dimensionless explanatory functions $h_i(\mathbf{x})$ and reads

$$\gamma(\mathbf{x}, \boldsymbol{\theta}) = \boldsymbol{\theta}^{\mathrm{T}} \cdot \mathbf{h}(\mathbf{x}). \tag{9}$$

The set of explanatory functions $\mathbf{h}(\mathbf{x}) = \{h_1(\mathbf{x}), .., h_n(\mathbf{x})\}$ is constructed starting from physical variables not included in $\hat{C}(\mathbf{x})$ that may be relevant for the described physical phenomenon, but also from those included in $\hat{C}(\mathbf{x})$ and the effect of which should be recalibrated in light of the available experimental data.

3.2. Bayesian approach for model calibration

The parameters collected into $\boldsymbol{\Theta}$ are calibrated using the Bayesian approach [89]. It combines the prior knowledge on the parameters, which is contained in the prior distribution of $\boldsymbol{\Theta}$, $f'(\boldsymbol{\Theta})$, with the information provided by the data, which is contained in the likelihood function, $\mathcal{L}(\boldsymbol{\Theta})$. The posterior distribution of the parameters $f''(\boldsymbol{\Theta})$ is defined as follows:

$$f''(\boldsymbol{\Theta}) = k\mathcal{L}(\boldsymbol{\Theta}) f'(\boldsymbol{\Theta}), \tag{10}$$

and it is obtained by dividing the product $\mathcal{L}(\boldsymbol{\Theta})f'(\boldsymbol{\Theta})$ by the evidence k, which is the following normalizing constant:

$$k^{-1} = \left[\int_{\Omega_{\boldsymbol{\Theta}}} \mathcal{L}(\boldsymbol{\Theta}) f'(\boldsymbol{\Theta}) \, \mathrm{d}\boldsymbol{\Theta}\right], \tag{11}$$

where $\Omega_{\boldsymbol{\Theta}}$ is the parameters space.

The posterior distributions $f''(\boldsymbol{\Theta})$ obtained after the calibration can be used to find a point estimate for the model by ignoring the epistemic uncertainties in the model parameters. An alternative approach is used in the present study, which also accounts for the epistemic uncertainties in the model parameters. This alternative approach assumes

$\mathbf{\Theta}$ as random variables and find a predictive estimate of $C(\mathbf{x}, \mathbf{\Theta})$ in agreement with [58] as follows:

$$\tilde{C}(\mathbf{x}) = \int\limits_{\Omega_{\mathbf{\Theta}}} C(\mathbf{x}; \mathbf{\Theta}) f''(\mathbf{\Theta}) \, \mathrm{d}\mathbf{\Theta}. \tag{12}$$

Since an analytical solution for Eq. (12) is often missing, it is opportune to find a numerical approximation of the distribution of $\tilde{C}(\mathbf{x})$ by sampling from $f''(\mathbf{\Theta})$ and finding the corresponding realizations of $C(\mathbf{x}; \mathbf{\Theta})$. In this way, it is possible to assume the sample mean of such realizations as predictive estimate and define the $\alpha\%$ confidence interval, where the lower and upper bounds are given by

$$\{0.5\,(100-\alpha)\,,\;\; [100-0.5\,(100-\alpha)]\}\,. \tag{13}$$

In this specific case, non-informative priors are chosen in the form of Gaussian distribution with zero means and large variance for all the parameters.

3.3. Stepwise deletion process for model selection

In order to facilitate the use of the model and its possible implementation into technical standards, it should be parsimonious (i.e., with a correction term constructed by means of a limited number of explanatory functions n) and as accurate as possible (i.e., with a small value of standard deviation σ). However, a reduction of n usually entails a higher value of σ. Stepwise deletion allows finding a compromise between parsimony and accuracy. There are several procedures to apply stepwise deletion, and they mostly differ in the deletion criteria, such as the stepwise deletion based on p-values [90]. The stepwise deletion process used in this paper starts with a model that includes all the candidate explanatory functions, and at each step removes the explanatory function with the highest coefficient of variation (COV) of the corresponding θ_i, as proposed in [58]. Once an explanatory function is removed, the model is re-calibrated and the deletion process repeated. The deletion process ends when either σ grows beyond an undesirable threshold, or the increment of σ is too large compared to the reduction of the model complexity.

3.4. Model for the axial capacity of CFST columns

The model of the axial capacity of CFST columns follows the form presented in Eq. (8). The modeled non-dimensional capacity parameter is $C(\mathbf{x}, \mathbf{\Theta}) = \tilde{N}_u(\mathbf{x}_u, \mathbf{\Theta}_u)/N_c$, i.e., the ratio between the axial capacity of CFST columns $\tilde{N}_u(\mathbf{x}_u, \mathbf{\Theta}_u)$ and the total compressive strength of the concrete core $N_c = f_c A_c$. For this model, the measurable capacity variables are $\mathbf{x}_u = \mathbf{s}$, and $\mathbf{\Theta}_u = \{\boldsymbol{\theta}_u, \sigma_u\}$ is the set of unknown model parameters. The variance stabilizing transformation used to approximately satisfy the additivity, normality, and homoskedasticity assumptions is the natural logarithm $T(\cdot) = \ln(\cdot)$ [89]. The chosen deterministic model is the ratio between the plastic compression resistance $N_{pl} = f_c A_c + f_y A_s$ and N_c, i.e., $\hat{C}(\mathbf{x}) = N_{pl}/N_c = 1 + \xi$. Consequently, Eq. (8) is rewritten as

$$\ln\left[\frac{\tilde{N}_u(\mathbf{x}_u, \mathbf{\Theta}_u)}{N_c}\right] = \ln(1+\xi) + \gamma_u(\mathbf{x}_u, \boldsymbol{\theta}_u) + \sigma_u \varepsilon, \tag{14}$$

or, equivalently, as

$$\ln\left[\frac{\tilde{N}_u(\mathbf{x}_u, \mathbf{\Theta}_u)}{N_{pl}}\right] = \gamma_u(\mathbf{x}_u, \boldsymbol{\theta}_u) + \sigma_u \varepsilon. \tag{15}$$

By means of this formulation, the axial capacity of the CFST column is expressed as follows:

$$\tilde{N}_u(\mathbf{x}_u, \mathbf{\Theta}_u) = N_{pl} \mathrm{e}^{[\gamma_u(\mathbf{x}_u, \boldsymbol{\theta}_u) + \sigma_u \varepsilon]}, \tag{16}$$

and the exponential factor derived from the correction term assumes the meaning of Strength Index (SI), which is a dimensionless parameter that quantifies the strength improvement of CFST columns due to the confinement effect and defined as the ratio N_u/N_{pl} [91]. Given the normality assumption, a 67% confidence interval for $\ln[\tilde{N}_u(\mathbf{x}_u, \mathbf{\Theta}_u)/N_c]$ can be found as follows:

$$\{\ln(1+\xi) + \gamma_u(\mathbf{x}_u, \boldsymbol{\theta}_u) - \sigma_u, \ln(1+\xi) + \gamma_u(\mathbf{x}_u, \boldsymbol{\theta}_u) + \sigma_u\}, \tag{17}$$

whereas the corresponding confidence interval for $\tilde{N}_u(\mathbf{x}_u, \mathbf{\Theta}_u)$ is

$$\left\{N_{pl} e^{[\gamma_u(\mathbf{x}_u, \boldsymbol{\theta}_u) - \sigma_u]}, N_{pl} e^{[\gamma_u(\mathbf{x}_u, \boldsymbol{\theta}_u) + \sigma_u]}\right\}. \tag{18}$$

Table 1 shows the set of non-dimensional candidate explanatory functions $h_{ui}(\mathbf{x}_u)$ used in the initial step of the stepwise deletion process. The first explanatory function $h_{u1}(\mathbf{x}_u)$

Table 1: Set of candidate explanatory functions for $\gamma_u\left(\mathbf{x}_u, \boldsymbol{\theta}_d\right)$.

Explanatory functions		
$h_{u1}(\mathbf{x}_u) = 1$	$h_{u6}(\mathbf{x}_u) = \psi$	$h_{u10}(\mathbf{x}_u) = \xi$
$h_{u2}(\mathbf{x}_u) = \lambda_r$	$h_{u7}(\mathbf{x}_u) = \lambda_r\psi$	$h_{u11}(\mathbf{x}_u) = \lambda_r\xi$
$h_{u3}(\mathbf{x}_u) = \lambda_r^2$	$h_{u8}(\mathbf{x}_u) = \lambda_r^2\psi$	$h_{u12}(\mathbf{x}_u) = \lambda_r^2\xi$
$h_{u4}(\mathbf{x}_u) = \lambda$	$h_{u9}(\mathbf{x}_u) = \lambda\psi$	$h_{u13}(\mathbf{x}_u) = \lambda\xi$
$h_{u5}(\mathbf{x}_u) = \frac{t}{D}$		$h_{u14}(\mathbf{x}_u) = \frac{t}{D}\xi$

takes into account a possible constant bias. The second and third explanatory functions, $h_{u2}(\mathbf{x}_u)$ and $h_{u3}(\mathbf{x}_u)$, are suggested by the formulation proposed by the Eurocode 4 [79] and are used to evaluate the possible effects of the relative slenderness λ_r defined as follows:

$$\lambda_r = \left(\frac{N_{pl}}{N_{cr}}\right)^{\frac{1}{2}}, \tag{19}$$

where

$$N_{cr} = \frac{\pi^2 EI_{eff}}{L^2} \tag{20}$$

is the elastic critical normal force for the relevant buckling mode, L is the length of the CFST column, and EI_{eff} is the characteristic value of the effective flexural stiffness of the cross-section given by

$$EI_{eff} = E_s I_s + 0.6 E_c I_c. \tag{21}$$

Herein, I_s and I_c are the second moments of area of the steel tube and concrete core, respectively. Moreover, E_s and E_c are the Young modulus of steel and concrete, respectively. Similarly, $h_{u4}(\mathbf{x}_u)$ explores the possible contribution of the geometric slenderness ratio $\lambda = L/D$, whereas $h_{u5}(\mathbf{x}_u)$ reflects the contribution of the relative thickness of steel tube and concrete core. The explanatory functions $h_{u6}(\mathbf{x}_u)$-$h_{u9}(\mathbf{x}_u)$ and $h_{u10}(\mathbf{x}_u)$-$h_{u14}(\mathbf{x}_u)$ search for the interactions between the same effects relevant for the explanatory functions $h_{u1}(\mathbf{x}_u)$-$h_{u5}(\mathbf{x}_u)$ and the contributions due to the confinement effect and steel tube (i.e., ψ and ξ, respectively).

3.5. Model of the eccentricity factor

The model for the reduction factor due to the eccentricity of the applied axial load is derived in the form given by Eq. (8) as follows:

$$\operatorname{logit}\left[\tilde{k}_e(\mathbf{x}_e, \mathbf{\Theta}_e)\right] = \ln\left[\frac{\tilde{k}_e(\mathbf{x}_e, \mathbf{\Theta}_e)}{1+\tilde{k}_e(\mathbf{x}_e, \mathbf{\Theta}_e)}\right] = \gamma_e\left(\mathbf{x}_e, \boldsymbol{\theta}_e\right) + \sigma_e\varepsilon. \tag{22}$$

In this case, there is no deterministic model, $\hat{C}(\mathbf{x}) = 0$, and the variance stabilizing transformation is the logit function $T(\cdot) = \operatorname{logit}(\cdot)$. The choice of the logit function approximately fulfills the three assumptions of the model and, at the same time, ensures that $\tilde{k}_e(\mathbf{x}_e, \mathbf{\Theta}_e) \in [0, 1]$. In Eq. (22), $\mathbf{x}_e = \{e, \mathbf{s}\}$ and $\mathbf{\Theta}_e = \{\boldsymbol{\theta}_e, \sigma_e\}$. The confidence interval for $\operatorname{logit}[\tilde{k}_e(\mathbf{x}_e, \mathbf{\Theta}_e)]$ can be found as

$$\left\{\gamma_e\left(\mathbf{x}_e, \boldsymbol{\theta}_e\right) - \sigma_e, \gamma_e\left(\mathbf{x}_e, \boldsymbol{\theta}_e\right) + \sigma_e\right\}, \tag{23}$$

whereas the confidence interval for $\tilde{k}_e(\mathbf{x}_e, \mathbf{\Theta}_e)$ is the following:

$$\left\{\frac{e^{[\gamma_e(\mathbf{x}_e,\boldsymbol{\theta}_e)-\sigma_e]}}{1-e^{[\gamma_e(\mathbf{x}_e,\boldsymbol{\theta}_e)-\sigma_e]}}, \frac{e^{[\gamma_e(\mathbf{x}_e,\boldsymbol{\theta}_e)+\sigma_e]}}{1-e^{[\gamma_e(\mathbf{x}_e,\boldsymbol{\theta}_e)+\sigma_e]}}\right\}. \tag{24}$$

Table 2 presents the non-dimensional candidate explanatory functions $h_{ei}(\mathbf{x}_e)$ that are included in the deletion process for $\tilde{k}_e(\mathbf{x}_e, \mathbf{\Theta}_e)$. Such explanatory functions can be divided into two subsets. The explanatory functions in the first subset, $h_{e1}(\mathbf{x}_e)$-$h_{e14}(\mathbf{x}_e)$, correspond to the explanatory functions $h_{u1}(\mathbf{x}_u)$-$h_{u14}(\mathbf{x}_u)$ used previously for modelling $\tilde{N}_u(\mathbf{x}_u, \mathbf{\Theta}_u)$. The other explanatory functions in the second subset, $h_{e15}(\mathbf{x}_e)$-$h_{e28}(\mathbf{x}_e)$, takes into account the possible interaction between the effects of the explanatory functions in the first subset and the non-dimensional eccentricity e/D, where the dimensional eccentricity $e = |e_{up} - e_{low}|$ is the absolute value of the difference between the eccentricity of the applied axial loads on the upper and lower bases of the CFST column, respectively.

3.6. Model of the debonding factor

The model of the debonding factor $\tilde{k}_d(\mathbf{x}_d, \mathbf{\Theta}_d)$ is limited to the circumferential debonding. However, the procedure presented in this paper can be applied without relevant changes to derive a model for the spherical-cap debonding. The model of $\tilde{k}_d(\mathbf{x}_d, \mathbf{\Theta}_d)$ is

Table 2: Set of candidate explanatory functions for $\gamma_e\left(\mathbf{x}_e, \boldsymbol{\theta}_e\right)$.

Explanatory functions without eccentricity		
$h_{e1}(\mathbf{x}_e) = 1$	$h_{e6}(\mathbf{x}_e) = \psi$	$h_{e10}(\mathbf{x}_e) = \xi$
$h_{e2}(\mathbf{x}_e) = \lambda_r$	$h_{e7}(\mathbf{x}_e) = \lambda_r\psi$	$h_{e11}(\mathbf{x}_e) = \lambda_r\xi$
$h_{e3}(\mathbf{x}_e) = \lambda_r^2$	$h_{e8}(\mathbf{x}_e) = \lambda_r^2\psi$	$h_{e12}(\mathbf{x}_e) = \lambda_r^2\xi$
$h_{e4}(\mathbf{x}_e) = \lambda$	$h_{e9}(\mathbf{x}_e) = \lambda\psi$	$h_{e13}(\mathbf{x}_e) = \lambda\xi$
$h_{e5}(\mathbf{x}_e) = \frac{t}{D}$		$h_{e14}(\mathbf{x}_e) = \frac{t}{D}\xi$
Explanatory functions with eccentricity		
$h_{e15}(\mathbf{x}_e) = \frac{e}{D}$	$h_{e20}(\mathbf{x}_e) = \psi\frac{e}{D}$	$h_{e24}(\mathbf{x}_e) = \xi\frac{e}{D}$
$h_{e16}(\mathbf{x}_e) = \lambda_r\frac{e}{D}$	$h_{e21}(\mathbf{x}_e) = \lambda_r\psi\frac{e}{D}$	$h_{e25}(\mathbf{x}_e) = \lambda_r\xi\frac{e}{D}$
$h_{e17}(\mathbf{x}_e) = \lambda_r^2\frac{e}{D}$	$h_{e22}(\mathbf{x}_e) = \lambda_r^2\psi\frac{e}{D}$	$h_{e26}(\mathbf{x}_e) = \lambda_r^2\xi\frac{e}{D}$
$h_{e18}(\mathbf{x}_e) = \lambda\frac{e}{D}$	$h_{e23}(\mathbf{x}_e) = \lambda\psi\frac{e}{D}$	$h_{e27}(\mathbf{x}_e) = \lambda\xi\frac{e}{D}$
$h_{e19}(\mathbf{x}_e) = \frac{te}{D^2}$		$h_{e28}(\mathbf{x}_e) = \frac{te}{D^2}\xi$

formally similar to that for $\tilde{k}_e(\mathbf{x}_e, \boldsymbol{\Theta}_e)$ in Eq. (22), and it reads

$$\operatorname{logit}\left[\tilde{k}_d(\mathbf{x}_d, \boldsymbol{\Theta}_d)\right] = \ln\left[\frac{\tilde{k}_d(\mathbf{x}_d, \boldsymbol{\Theta}_d)}{1+\tilde{k}_d(\mathbf{x}_d, \boldsymbol{\Theta}_d)}\right] = \gamma_d\left(\mathbf{x}_d, \boldsymbol{\theta}_d\right) + \sigma_d\varepsilon, \tag{25}$$

where $\mathbf{x}_d = \{\mathbf{d}, \mathbf{s}\}$, $\mathbf{d} = \{T_d, R_d, L_d\}$, and $\boldsymbol{\Theta}_d = \{\boldsymbol{\theta}_d, \sigma_d\}$. Also the confidence intervals for $\operatorname{logit}[\tilde{k}_d(\mathbf{x}_d, \boldsymbol{\Theta}_d)]$ and $\tilde{k}_d(\mathbf{x}_d, \boldsymbol{\Theta}_d)$ are analogous to those presented in Eq. (23) and Eq. (24), respectively. As shown in Table 3, the non-dimensional explanatory functions considered as candidates for $\tilde{k}_d(\mathbf{x}_d, \boldsymbol{\Theta}_d)$ are mostly functions of the geometric characteristics of the debonding. Among the explanatory functions in the first column of Table 3, $h_{d1}(\mathbf{x}_d)$ accounts for a possible constant bias, $h_{d2}(\mathbf{x}_d)$ is proportional to the slenderness of the CFST columns, and $h_{d3}(\mathbf{x}_d)$-$h_{d8}(\mathbf{x}_d)$ are directly related to geometric characteristics of the debonding. In particular, $h_{d7}(\mathbf{x}_d)$ investigates the possible dependence of the debonding factor on the the volume of the gap between the two materials, whereas $h_{d8}(\mathbf{x}_d)$ accounts for the area of the surface where the concrete core and the steel tube are detached. The two subsets of explanatory functions $\{h_{d3}, h_{d11}, h_{d19}\}$ and $\{h_{d4}, h_{d12}, h_{d20}\}$ are both related to the debonding thickness T_d. In the first subset, T_d is scaled by the outer diameter of the CFST column, whereas the characteristic value of the debonding thickness $T^* = 3$ mm [49, 88] is considered in the second subset. The two subsets are considered as alternatives and not included at the same time in the model selection. Explanatory functions

$h_{d9}(\mathbf{x}_d)$-$h_{d14}(\mathbf{x}_d)$ and $h_{d17}(\mathbf{x}_d)$-$h_{d22}(\mathbf{x}_d)$ analyse the interaction between the effects captured by $h_{d1}(\mathbf{x}_d)$-$h_{d6}(\mathbf{x}_d)$ and the contributions due to ψ and ξ, respectively. In $h_{d15}(\mathbf{x}_d)$ and $h_{d16}(\mathbf{x}_d)$, D_{min} and L_{min} are the minimum values of diameter end height among those of the specimens in the dataset used for model calibration.

Table 3: Set of candidate explanatory functions for $\gamma_u\left(\mathbf{x}_d, \boldsymbol{\theta}_d\right)$.

Explanatory functions		
$h_{d1}(\mathbf{x}_d) = 1$	$h_{d9}(\mathbf{x}_d) = \psi$	$h_{d17}(\mathbf{x}_d) = \xi$
$h_{d2}(\mathbf{x}_d) = \lambda$	$h_{d10}(\mathbf{x}_d) = \lambda\psi$	$h_{d18}(\mathbf{x}_d) = \lambda\xi$
$h_{d3}(\mathbf{x}_d) = \frac{T_d}{D}$	$h_{d11}(\mathbf{x}_d) = \frac{T_d}{D}\psi$	$h_{d19}(\mathbf{x}_d) = \frac{T_d}{D}\xi$
$h_{d4}(\mathbf{x}_d) = \frac{T_d}{T^*}$	$h_{d12}(\mathbf{x}_d) = \frac{T_d}{T^*}\psi$	$h_{d20}(\mathbf{x}_d) = \frac{T_d}{T^*}\xi$
$h_{d5}(\mathbf{x}_d) = R_d$	$h_{d13}(\mathbf{x}_d) = R_d\psi$	$h_{d21}(\mathbf{x}_d) = R_d\xi$
$h_{d6}(\mathbf{x}_d) = \frac{L_d}{L}$	$h_{d14}(\mathbf{x}_d) = \frac{L_d}{L}\psi$	$h_{d22}(\mathbf{x}_d) = \frac{L_d}{L}\xi$
$h_{d7}(\mathbf{x}_d) = R_d\frac{L_d}{L}\frac{T_d}{D}$	$h_{d15}(\mathbf{x}_d) = \frac{D}{D_{min}}$	$h_{d23}(\mathbf{x}_d) = R_d\frac{L_d}{L}\frac{T_d}{D}\xi$
$h_{d8}(\mathbf{x}_d) = R_d\frac{L_d}{L}$	$h_{d16}(\mathbf{x}_d) = \frac{L}{L_{min}}$	

4. Model calibration and model selection

For all models, the calibration is performed at each stage of the model selection process with the STAN package of the R software [92] that uses a gradient descend method. Two extensive databases, recently analysed in [13] and [60], are used to calibrate the models for $\tilde{N}_u(\mathbf{x}_u, \mathbf{\Theta}_u)$ and $\tilde{k}_e(\mathbf{x}_e, \mathbf{\Theta}_e)$, and the model for $\tilde{k}_d(\mathbf{x}_d, \mathbf{\Theta}_d)$, respectively.

4.1. Calibration and selection of the axial capacity model

The model $\tilde{N}_u(\mathbf{x}_u, \mathbf{\Theta}_u)$ is calibrated with records from the database analysed in [13]. The database contains tests conducted on both rectangular and circular CFST columns and includes data obtained from specimens with high-strength materials and slender sections. Some of the data are collected from tests where the normal force is applied in an eccentric position (i.e., tests where the members are subjected to combined axial compression and bending moment). Only data from tests without eccentricity of the applied axial loads and CFST columns with circular cross-section are herein used for the calibration of $\tilde{N}_u(\mathbf{x}_u, \mathbf{\Theta}_u)$, thereby resulting in a total of 815 records.

Figure 1 presents the results of the stepwise deletion process for the axial capacity model. For each step, the figure shows the value for the posterior mean of σ_u, which is

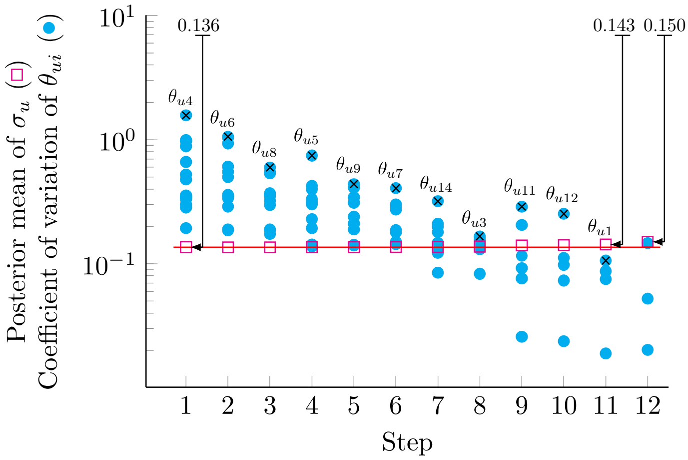

Figure 1: Stepwise deletion process for the axial capacity model.

represented by a square, and the coefficients of variation of the θ_{ui}'s related to the h_{ui}'s included at that step, which are represented by dots. The dots with a cross denote the coefficients of variation of the terms that are dropped. The red line represents the value of σ_u at the first step, and it is used to facilitate the comparison with the values of σ_u in the following steps. The figure also explicitly shows the values of σ_u at some selected steps. In the first step, the selection process removes h_{u4}, which is the term associated to the parameter with the largest coefficient of variation, θ_{u4}, being $\mathrm{COV}_{\theta_{u4}} = 1.57$. One term is removed at each step up to Step 10, which leads to the elimination of θ_{u12} and a 5% cumulative increase in σ_u. The process stops at Step 11 because removing h_{u1} would result in a cumulative increase in σ_u higher than 10%, which is deemed excessive, and because the additional step would entail an increase in σ_u equivalent to the cumulative increase of the first 10 steps. The 10% threshold is chosen to have a parsimonious model that could be adopted in technical standards. Moreover, the difference in accuracy between the reduced model and the full model (i.e., the model obtained without applying the stepwise deletion process) is limited. The reduced model resulting from the selection process has $\gamma_u(\mathbf{x}_u, \boldsymbol{\theta}_u)$ in the following form:

$$\gamma_u\left(\mathbf{x}_u, \boldsymbol{\theta}_u\right) = \theta_{u0} + \theta_{u2}\lambda_r + \left(\theta_{u10} + \theta_{u14}\frac{t}{D}\right)\xi. \tag{26}$$

This formulation suggests that there may be a systematic bias in the deterministic predictions obtained with N_{pl} because h_{u1} is retained in the model. It also shows that λ_r plays

Table 4: Posterior statistics of $\mathbf{\Theta}_u$

$\mathbf{\Theta}_u$	Mean	Stand. dev.	Correlation coefficients				
			θ_{u1}	θ_{u2}	θ_{u10}	θ_{u14}	σ_u
θ_{u1}	0.12	0.01	1.00	—	—	—	—
θ_{u2}	−0.97	0.02	−0.34	1.00	—	—	—
θ_{u10}	0.10	0.01	−0.59	−0.25	1.00	—	—
θ_{u14}	−0.79	0.08	0.47	0.20	−0.92	1.00	—
σ_u	0.14	0.01	−0.01	0.01	0.01	−0.01	1.00

a significant role in reducing the axial capacity of CFST columns. The combined effect of h_{u10} and h_{u14} likely accounts for the confinement effect, which is proportional to the compressive strength of the steel column and depends on the t/D ratio. Table 4 gives the posterior statistics of the five model parameters.

Figure 2 shows the predicted versus measured capacity for each test. The closer the data points are to the 1:1 lines (i.e., the continuous lines in the figure), the more accurate are the predictions. Figures 2(a) and 2(c) compare predictions made considering the plastic resistance to compression. In this case, the predictions underestimate the axial capacity at high values of N_u. Figures 2(b) and 2(d) show the predictions modified by $\gamma_u(\mathbf{x}_u, \boldsymbol{\theta}_u)$. Such predictions are median values obtained by considering the posterior statistics of $\boldsymbol{\theta}_u$ and $\varepsilon_u = 0$. The proposed model provides more accurate predictions since the data points are closer to the 1:1 lines. Figures 2(b) and 2(d) also show the region within one standard deviation of the median value, which is the region enclosed by the dashed lines.

4.2. Calibration and selection of the eccentricity factor model

The model of $\tilde{k}_e(\mathbf{x}_e, \mathbf{\Theta}_e)$ is calibrated with records from the same dataset used to calibrate $\tilde{N}_u(\mathbf{x}_u, \mathbf{\Theta}_u)$ but retaining only data from CFST columns with circular cross-section and eccentric axial load (i.e., $e > 0$). Additionally, model calibration and model selection are performed by considering only the 83 data points with $e/D < 0.15$ to ensure that the CFST column specimens are mostly subjected to compression. It is pointed out that similar limits are also adopted by technical standards (e.g., the use of the formulation proposed by the Eurocode 4 [79] is limited to CFST columns with $e/D < 0.1$). The dataset used to calibrate the model only provides the axial capacity of the specimens N_{ue}, not the values for k_e. In order to derive k_e, the axial capacity N_u of CFST columns having the same geometry and material characteristics of the specimens used in the tests

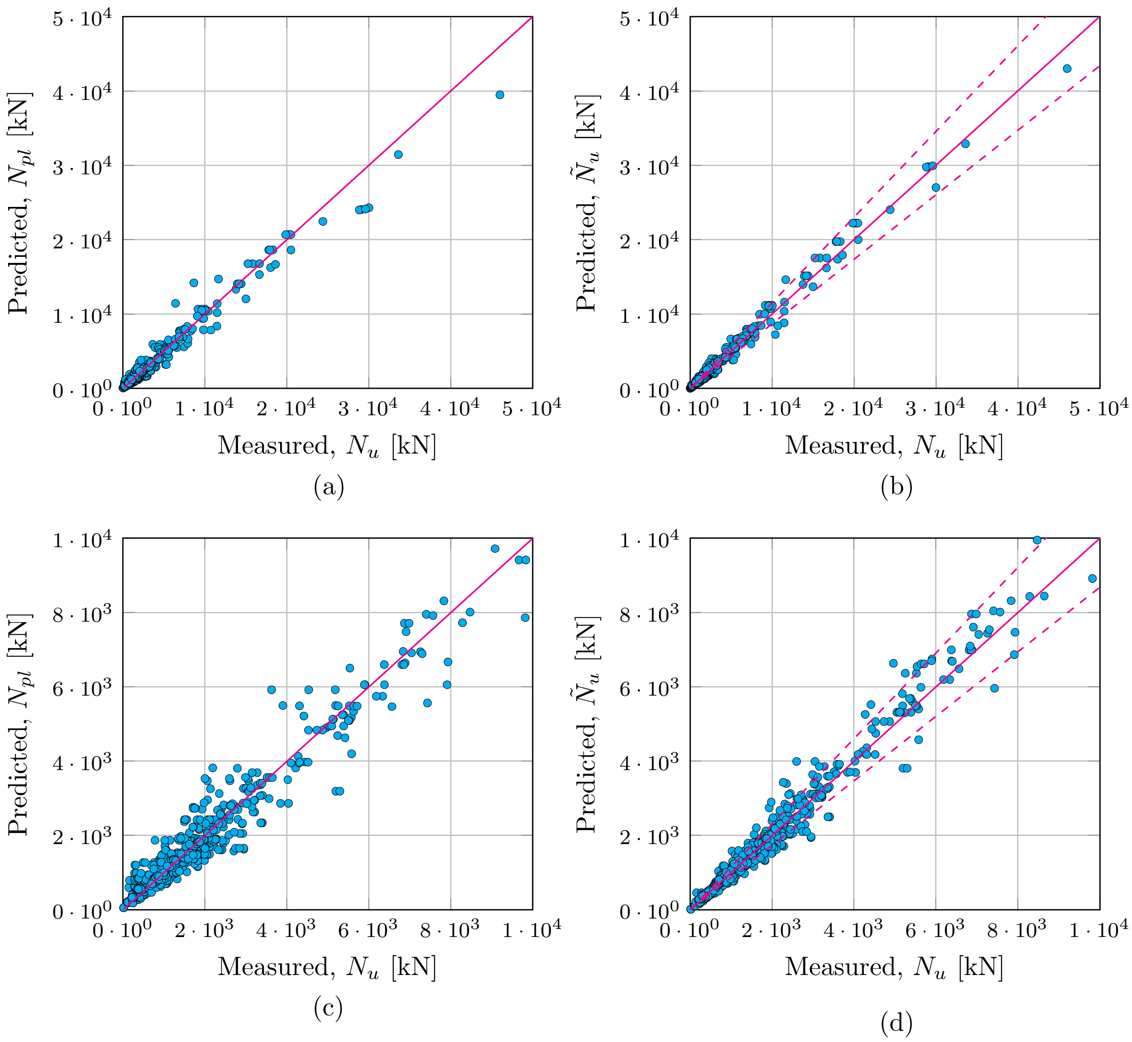

Figure 2: Predicted versus measured values of the axial capacity: (a-c) predictions with plastic resistance to compression; (b-d) predictions with proposed probabilistic model.

and without the eccentricity of the applied axial load is predicted with the probabilistic model proposed previously. With such predictions, the eccentricity factor is derived as $k_e = N_{ue}/\tilde{N}_u(\mathbf{x}_u, \hat{\mathbf{\Theta}}_u)$, where $\hat{\mathbf{\Theta}}_u$ is the vector of the mean values of the parameters in Table 4.

Figure 3 presents the results of the stepwise deletion process for the eccentricity factor model. The deletion process stops after the removal of h_{e10} at Step 22 because the removal of h_{e7} at Step 23 would caused a a cumulative increase in σ_u higher than 20%, which is deemed undesirable. Therefore, h_{e7} is kept in the final form of $\gamma_e(\mathbf{x}_e, \boldsymbol{\theta}_e)$, which reads

$$\gamma_e\left(\mathbf{x}_e, \boldsymbol{\theta}_e\right) = \theta_{e0} + \theta_{e2}\lambda_r + \theta_{e4}\lambda + \left(\theta_{e7}\lambda_r + \theta_{e9}\lambda\right)\psi + \theta_{e15}\frac{e}{D}. \tag{27}$$

Equation 27 and the posterior statistics of the model parameters in Table 5 show that both λ_r and λ provide significant contributions to the value of k_e. Since $0.008 < \psi < 0.635$ for the tests used in the model calibration, the effect of λ_r is the one of reducing k_e, whereas λ contributes to increase k_e. As expected, the retained explanatory function that includes the eccentricity, h_{e15}, reduces the value of k_e.

Table 5: Posterior statistics of $\mathbf{\Theta}_e$.

$\mathbf{\Theta}_e$	Mean	Stand. dev.	Correlation coefficients						
			θ_{e1}	θ_{e2}	θ_{e4}	θ_{e7}	θ_{e9}	θ_{e15}	σ_e
θ_{e1}	2.635	0.197	1.00	—	—	—	—	—	—
θ_{e2}	−14.813	2.536	−0.59	1.00	—	—	—	—	—
θ_{e4}	0.509	0.084	0.57	−0.99	1.00	—	—	—	—
θ_{e7}	34.285	12.824	0.41	−0.76	0.69	1.00	—	—	—
θ_{e9}	−1.334	0.390	−0.43	0.81	−0.75	−0.99	1.00	—	—
θ_{e15}	−13.628	1.874	−0.89	0.50	−0.53	−0.26	0.29	1.00	—
σ_e	0.433	0.036	−0.01	0.01	−0.01	−0.01	0.01	−0.01	1.00

Figures 4(a) and (b) show the predicted versus measured values of k_e in the transformed and original space, respectively. As in Fig. 2, the continuous line is the 1:1 line and the dashed lines represent the upper and lower bounds of the region within one standard deviation from the median value. Although the model seems to slightly underestimate the highest values of k_e, the results show good accuracy of the final predictions. The model may also be affected by the high variability of the experimental data.

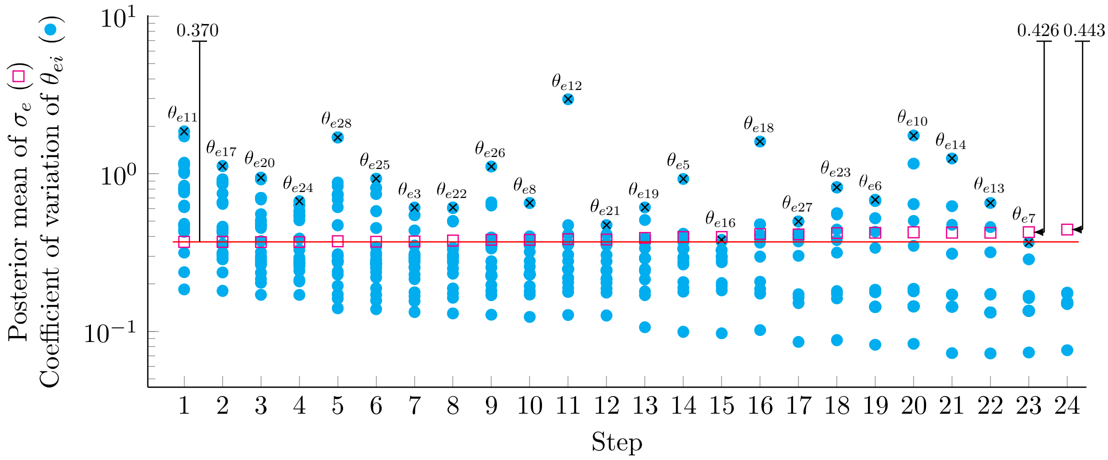

Figure 3: Stepwise deletion process for the eccentricity factor model.

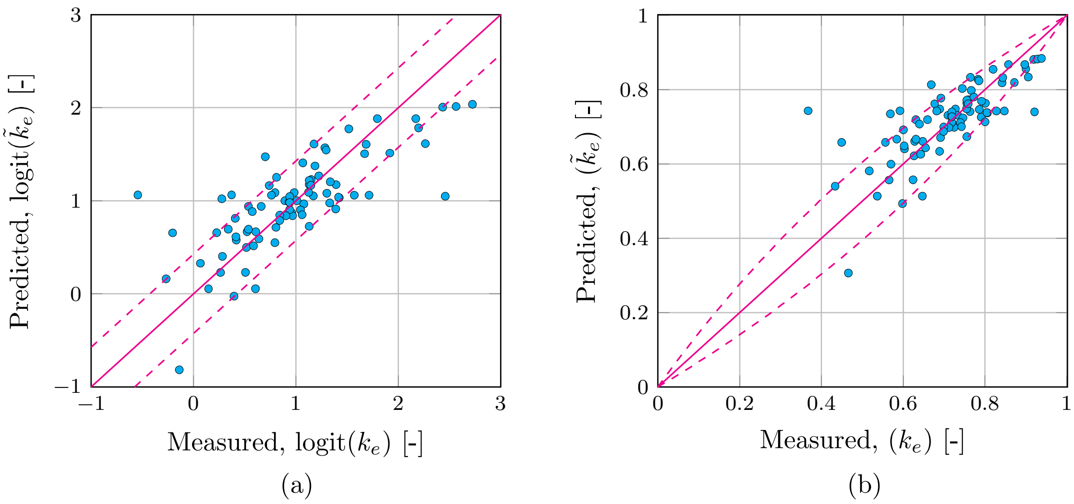

Figure 4: Predicted eccentricity factor versus measured eccentricity factor: (a) transformed space; (b) original space.

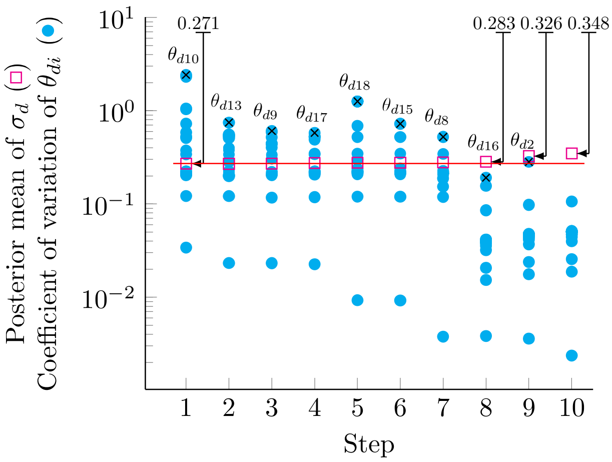

Figure 5: Stepwise deletion process for the debonding factor model.

4.3. Calibration and selection of the debonding factor model

The database presented in [60] is used to calibrate $\tilde{k}_d(\mathbf{x}_d, \mathbf{\Theta}_d)$. Also in this case, only data from CFST columns with circular cross-section are used for the calibration, which amount to 93 records. Figure 5 shows the stepwise deletion process for the debonding factor model. The last removed term is h_{d16}: its elimination at Step 9 leads to reach the threshold of 20% cumulative increase in σ_d. From a statistical point of view, the stepwise deletion process could have been stopped at Step 8, after a 4% cumulative increase in σ_d. However, the resulting formulation would have included an explanatory function, h_{d16}, that would limit the range of applicability of the model to columns with $L > L_{min}$. Therefore, a further step (i.e., the continuation of the process up to Step 9) is preferred. The model derived from the stepwise deletion process is the following:

$$\gamma_d(\mathbf{x}_d, \boldsymbol{\theta}_d) = \theta_{d1} + \theta_{d2}\lambda + (\theta_{d3} + \theta_{d11}\psi + \theta_{d19}\xi)\frac{T_d}{D} + (\theta_{d5} + \theta_{d21}\xi) R_d + (\theta_{d6} + \theta_{d14}\psi + \theta_{d22}\xi)\frac{L_d}{L} + (\theta_{d7} + \theta_{d23}\xi) R_d \frac{T_d}{D}\frac{L_d}{L} \tag{28}$$

Such a model includes more terms than the models selected for $\tilde{N}_u(\mathbf{x}_u, \boldsymbol{\Theta}_u)$ and $\tilde{k}_e(\mathbf{x}_e, \boldsymbol{\Theta}_e)$. However, removing any other term from Eq. (28) would lead to a significant increase in σ_d with a consequent large reduction of the predicting capability of the model. Equation (28) shows that all the geometric characteristics of debonding phenomenon (i.e., T_d, R_d, and L_d) does matter to evaluate the reduction of the axial capacity due to debonding. The survival of two terms related to the volume of the debonding gap, h_{d7} and h_{d23}, can be related to a reduction in the confinement effect. Such a reduction can be explained considering that, in the intermediate phase of the loading process of the CFST columns, a larger increment of the concrete micro-cracking is needed to mobilize the steel tube and start the confinement effect. The only two explanatory functions not directly related to debonding are h_{d1}, which is a constant, and h_{d2}, which is the geometric slenderness of the CFST column. The two terms have opposite effects: while h_{d1} increases the value of k_d, h_{d2} reduces the value of k_d for CFST columns with large slenderness. Table 6 presents the statistics of the parameters that multiply the explanatory functions in Eq. (28).

Figure 6 shows the predicted versus measured values of k_d. Figures 6(a) and (b) are presented in the transformed and original spaces, respectively. The perfect agreement between test values and predictions as well as the bounds of the region within one standard deviation form the median value are represented with solid and dashed lines, respectively. Despite a single case which is significantly under-predicted, the model seems to be unbiased. The model is particularly accurate in the prediction of cases that have the debonding length smaller than the length of the CFST column and a limited reduction of the axial capacity.

Table 6: Posterior statistics of $\mathbf{\Theta}_d$.

$\mathbf{\Theta}_d$	θ_{d1}	θ_{d2}	θ_{d3}	θ_{d5}	θ_{d6}	θ_{d7}	θ_{d11}	θ_{d14}	θ_{d19}	θ_{d21}	θ_{d22}	θ_{d23}	σ_d
Mean	$3.024 \cdot 10^{1}$	$-6.632 \cdot 10^{-2}$	$-3.555 \cdot 10^{3}$	$-8.918 \cdot 10^{1}$	$1.821 \cdot 10^{1}$	$6.532 \cdot 10^{3}$	$1.742 \cdot 10^{6}$	$-2.297 \cdot 10^{4}$	$-4.237 \cdot 10^{5}$	$8.882 \cdot 10^{1}$	$5.589 \cdot 10^{3}$	$-6.706 \cdot 10^{3}$	$3.310 \cdot 10^{-1}$
Stand. dev.	$1.110 \cdot 10^{-1}$	$1.920 \cdot 10^{-2}$	$1.503 \cdot 10^{2}$	$1.598 \cdot 10^{0}$	$1.812 \cdot 10^{0}$	$1.589 \cdot 10^{2}$	$7.847 \cdot 10^{4}$	$1.116 \cdot 10^{3}$	$1.901 \cdot 10^{4}$	$3.342 \cdot 10^{0}$	$2.712 \cdot 10^{2}$	$3.193 \cdot 10^{2}$	$2.652 \cdot 10^{-2}$
	Correlation coefficients												
$\mathbf{\Theta}_d$	θ_{d1}	θ_{d2}	θ_{d3}	θ_{d5}	θ_{d6}	θ_{d7}	θ_{d11}	θ_{d14}	θ_{d19}	θ_{d21}	θ_{d22}	θ_{d23}	σ_d
θ_{d1}	1.00	—	—	—	—	—	—	—	—	—	—	—	—
θ_{d2}	−0.79	1.00	—	—	—	—	—	—	—	—	—	—	—
θ_{d3}	−0.03	−0.01	1.00	—	—	—	—	—	—	—	—	—	—
θ_{d5}	−0.21	0.15	0.78	1.00	—	—	—	—	—	—	—	—	—
θ_{d6}	0.07	−0.06	−0.94	−0.81	1.00	—	—	—	—	—	—	—	—
θ_{d7}	0.14	−0.09	−0.81	−0.83	0.72	1.00	—	—	—	—	—	—	—
θ_{d11}	0.05	−0.02	−0.78	−0.51	0.83	0.49	1.00	—	—	—	—	—	—
θ_{d14}	−0.08	0.05	0.71	0.49	−0.82	−0.48	−0.97	1.00	—	—	—	—	—
θ_{d19}	−0.05	0.02	0.78	0.51	−0.82	−0.49	−0.98	0.97	1.00	—	—	—	—
θ_{d21}	0.12	−0.09	−0.71	−0.97	0.72	0.83	0.34	−0.32	−0.33	1.00	—	—	—
θ_{d22}	0.08	−0.05	−0.71	−0.48	0.81	0.48	0.97	−0.98	−0.97	0.31	1.00	—	—
θ_{d23}	−0.07	0.05	0.75	0.86	−0.65	−0.97	−0.34	0.31	0.33	−0.90	−0.30	1.00	—
σ_d	−0.01	0.01	0.01	0.01	−0.01	0.01	−0.01	0.01	−0.01	−0.01	−0.01	−0.01	1.00

May 23, 2022

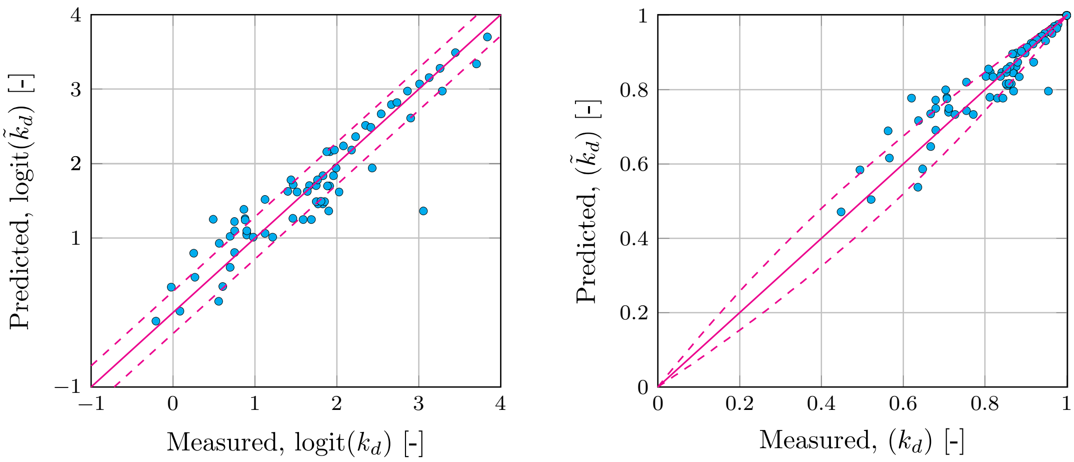

(a) (b)

Figure 6: Predicted debonding factor versus measured debonding factor: (a) transformed space; (b) original space.

4.4. Comparison with models from technical standards and literature

Figure 7 presents a comparative assessment of the axial capacity of CFST columns in terms of the ratio between numerical predictions and corresponding experimental values $r_u = N_u^{\text{pre}}/N_u^{\text{exp}}$. The figure presents both predictions made with code-conforming formulations [49, 77, 79, 93] and with formulations from the literature [47, 78, 94]; both groups are presented in chronological order. A short presentation of these formulations is provided in Appendix. This assessment is intended to analyse the differences between the formulations and should not be considered as a competitive evaluation of their accuracy. This is because the existing formulations considered for the present comparative assessment might have been developed on a testing dataset instead of the complete dataset, or because the code-conforming formulations require design values and are not intended for mean values, or even because the considered formulations may not be valid for the intervals of the parameters in the considered dataset.

Table 7 shows the statistics of the distributions of r_u, the Mean Absolute Error (MAE), the Root Mean Square Error (RMSE), and the Variance Accounted For (VAF) obtained from the different formulations considered in the comparative assessment. It can be observed from Fig. 7 and Table 7 that all code-conforming formulations tend to underestimate the axial capacity of CFST columns. The formulations collected from the existing literature show a progressive increment of accuracy in time. Overall, the statistical indicators used

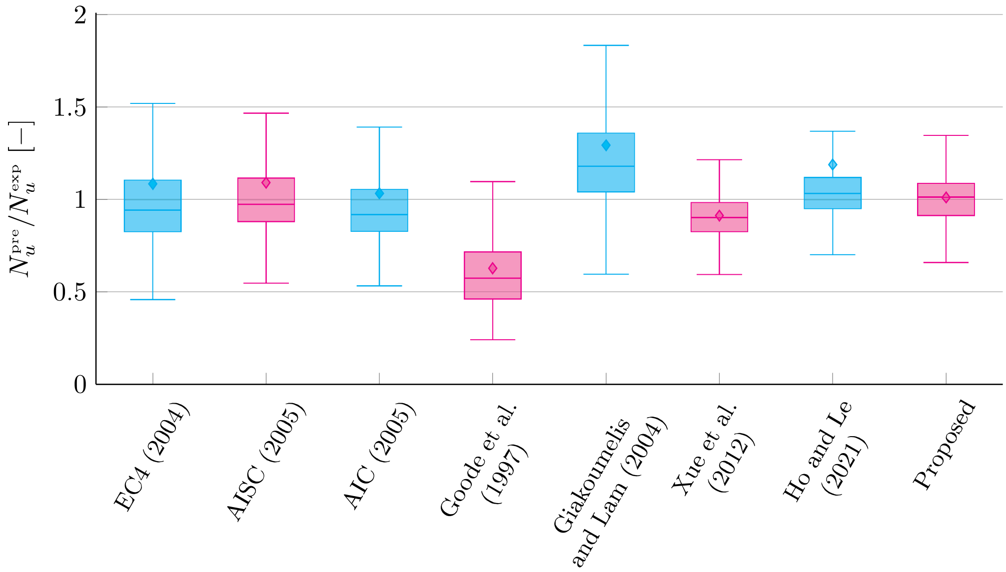

Figure 7: Comparison among predictions of the axial capacity of CFST columns in terms of box plot of the ratio between numerical predictions and corresponding experimental values $N_u^{\mathrm{pre}}/N_u^{\mathrm{exp}}$ (complete dataset of 815 samples).

for the comparative assessment show a moderate increment of the accuracy level obtained by means of the proposed model. Specifically, mean and standard deviation of the ratio between predicted and experimental values according to the proposed models are slightly better than those carried out by means of the most recent formulations, while MAE and RMSE have improved to a greater extent. The main difference with the earliest formulations [47, 78] is the lack of the confinement effect, which is either not considered (in [78]) or overestimated (in [47]).

Table 7: Mean, standard deviation and mean squared error of the ratio between numerical predictions and corresponding experimental values $N_u^{\mathrm{pre}}/N_u^{\mathrm{exp}}$ (complete dataset of 815 samples), Mean Absolute Error (MAE), Root Mean Square Error (RMSE), and Variance Accounted For (VAF).

Formulation	$N_u^{\mathrm{pre}}/N_u^{\mathrm{exp}}$			MAE [kN]	RMSE [kN]	VAF %
	Mean	Standard deviation	Mean square error			
EC4 (2004)	1.084	0.593	0.359	425.748	935.777	94.866
AISC (2005)	1.091	0.472	0.231	342.902	742.282	96.707
ACI (2005)	1.033	0.453	0.206	411.129	888.189	95.540
Goode et al. (1997)	0.627	0.284	0.219	1031.22	2263.43	75.029
Giakoumelis and Lam (2004)	1.293	0.546	0.384	548.974	1051.80	94.310
Xue et al. (2013)	0.912	0.189	0.044	326.230	733.983	97.135
Ho and Le (2021)	1.188	0.230	0.056	248.992	562.408	98.127
Proposed	1.011	0.155	0.024	229.267	452.192	98.769

A similar comparative assessment can be done in terms of the ratio between numerical predictions and corresponding experimental values in case of eccentric applied axial load $r_e = N_{ue}^{\text{pre}}/N_{ue}^{\text{exp}}$. In this case, the comparison can be made with the formulation included into Eurocode 4 only, which directly provides the formulation to estimate N_{ue}. On the other hand, two prediction steps are needed when using the proposed formulation. In the first step, N_u is predicted using the model in Eq. 16 by disregarding the effect of the eccentricity of the applied axial load. In the second step, the predicted value of N_u is reduced using the predictions of k_e carried out from Eq. 22. Mean value, standard deviation, and mean squared error of r_e obtained with the proposed formulation (i.e., $\mu_{re} = 1.049$, $\sigma_{re} = 0.204$, and $MSE_{re} = 0.043$) are consistently smaller than those obtained with the formulation provided by Eurocode 4 (i.e., $\mu_{re} = 1.637$, $\sigma_{re} = 1.049$, and $MSE_{re} = 1.642$). Such a difference can be justified, to some extent, by recalling that the predictions are made using the mean values for the material strength parameters and the non-dimensional eccentricity range in the dataset is $e/D < 0.15$ while the validity of the formulation in the Eurocode 4 is limited to $e/D < 0.1$.

A further comparative assessment is done for k_d. Such comparative assessment is made between the results proposed in this paper and those presented by Xue et al. [60], which were derived on the same experimental dataset and were specifically intended for circumferential debonding. The formulation provided in [60] for k_d reads

$$k_d = 0.9947 - 3.4871 \frac{L^{\frac{1}{6}} (R_d T_d L_d)^{\frac{1}{3}}}{D^{\frac{1}{6}} t^{\frac{2}{3}} f_y^{\frac{1}{6}} f_c}, \tag{29}$$

and was obtained by means of a machine learning-based approach (namely, the Evolutionary Polynomial Regression technique). Since both results are already expressed in terms of k_d, there is no need to shift the comparison on the corresponding axial capacities. Once again, the comparison is based on the ratio between numerical predictions and corresponding experimental values $r_d = k_d^{\text{pre}}/k_d^{\text{exp}}$. This further comparative assessment demonstrates that the two formulations have equivalent accuracy. Mean value, standard deviation and mean squared error of r_d obtained with the proposed formulation are $\mu_{rd} = 1.009$, $\sigma_{rd} = 0.064$, and $MSE_{rd} = 0.035$, whereas those obtained with the formulation in [60] are $\mu_{rd} = 1.012$, $\sigma_{rd} = 0.057$, and $MSE_{rd} = 0.035$. The main difference between the two formulations is that the one presented herein is mechanics-based and, as a consequence, is likely to be more robust (i.e., its accuracy degrades slower when considering data outside the ranges of the corresponding values used for model calibration). Additionally, since the proposed model is calibrated with a Bayesian approach, its coefficients can be updated to include information coming from new tests. Conversely, the formulation presented in [60] is more compact.

5. Derivation of uncertainty factors for design applications

The potential use of the proposed formulation for practical applications requires the definition of an uncertainty factor γ_{Nd} for the calculation of the design value of the axial capacity. Such uncertainty factor is needed to avoid the underestimation of the axial capacity due to the involved uncertainties, in such a way that the design can ensure a safety margin in compliance with code regulations. The code-format design axial capacity can be defined as follows:

$$N_{ud} = \frac{\eta}{\gamma_{Nd}} \tilde{N}_u \left(\mathbf{x}_{ud}, \boldsymbol{\Theta}_u\right), \tag{30}$$

where η is a conversion factor that depends on the technical standard [79] and $\mathbf{x}_{ud}$ is the vector of the design values of the capacity variables. In a similar fashion, for CFST columns with axial load applied in eccentric position or with debonding, the code-format design axial capacity reads

$$N_{ud} = \frac{\eta}{\gamma_{Nd}} \tilde{k}_e \left(\mathbf{x}_{ed}, \boldsymbol{\Theta}_e\right) \tilde{N}_u \left(\mathbf{x}_{ud}, \boldsymbol{\Theta}_u\right) \tag{31}$$

and

$$N_{ud} = \frac{\eta}{\gamma_{Nd}} \tilde{k}_d \left(\mathbf{x}_{dd}, \boldsymbol{\Theta}_d\right) \tilde{N}_u \left(\mathbf{x}_{ud}, \boldsymbol{\Theta}_u\right), \tag{32}$$

respectively. The estimation of γ_{Nd} is performed by assuming that the design value is less than the corresponding experimental value with a probability equal to p as

$$P \left[N_{ud} < N_u^{\exp}\right] = p \tag{33}$$

The value of p depends on the reference technical standard. The estimation of γ_{Nd} is performed with $\eta = 1$ and characteristic values of compressive concrete strength and steel yielding stress equal to those in the experimental database used for the model calibration. The ratio of the number of samples for which $N_{ud} > N_u^{\exp}$ and the total number of samples is used to estimate $P[N_{ud} < N_u^{\exp}]$ and the corresponding value of γ_{Nd}. Table 8 compares the values of γ_{Nd} obtained for three different technical standards, namely Eurocodes, AASHSTO, and GB50923-2013. The European building code sets p as $\Phi(\alpha_R \beta_{LS})$, where $\Phi(\cdot)$ is the standard Normal cumulative distribution function, α_R is the sensitivity factor for the capacity, and β_{LS} is the safety index relevant to the considered limit state. Assuming a 50-years reference period and an ultimate limit state, $\Phi(\alpha_R \beta_{LS})$=0.9988. For AASHSTO, the value of p is derived as $p = \Phi(3.5) = 0.9997$ because $\beta = 3.5$ is the target reliability index. In accordance with the specifications of the GB50923-2013 technical standard, the value of p is derived assuming a ductile failure and the 2nd safety level, which lead to $p = \Phi(3.2) = 0.9993$.

The calibration of γ_{Nd} is performed with all available data, including those with eccentric applied axial load and debonding. The accuracy in approaching the target values of p and, consequently, in defining an accurate value of γ_{Nd} is determined by both the number of available samples and the distribution of $N_u^{\exp}$. Since 1006 tests are used, the probability values closer to the target values of p are $p^* = 1004/1006 = 0.9980$, $p^* = 1005/1006 = 0.9990$, and $p^* = 1006/1006 = 1.000$. The values of γ_{Nd} corresponding to the target values of p are obtained by linear interpolation. Table 8 shows the results of the calibration.

Table 8: Model uncertainty factors for γ_{Nd} for the proposed axial capacity derived according to the three different technical standards.

Technical standard	Target value of p	γ_{Nd} for $p^* = 0.9980$	γ_{Nd} for $p^* = 0.9990$	γ_{Nd} for $p^* = 1.0000$	Interpolated γ_{Nd}
EC4	0.9988	1.599	1.815	—	1.772
AASHTO	0.9997	—	2.276	3.128	2.872
GB50923-2013	0.9993	—	1.642	2.484	1.895

The higher values of γ_{Nd} derived for the AASHTO compared to those obtained for the Eurocode 4 and GB50923-2013 are due to both the higher target reliability index and the higher design values of the compressive concrete strength and steel yielding stress.

6. Conclusions

The beneficial interaction between steel tube and infilled concrete core has promoted the large diffusion of CFST columns in many projects over the years. To begin with, the concrete core prevents inward local buckling of the steel tube. At the same time, the steel tube confines the concrete core. Such synergy results in high load-carrying capacity and enhanced ductility, that come together with economic and construction efficiency benefits due to the use of the steel tube as permanent formwork. Motivated by these attractive features, a large amount of experimental, analytical, and numerical studies about CFST columns under axial load have been performed in the last decades, but a probabilistic capacity model has not been proposed yet. Furthermore, there is still a lack of researches about the quantification of the effects due to load eccentricity and debonding. Hence, the present study is meant at filling this gap and, to this end, proposed a comprehensive probabilistic model for the axial capacity of CFST columns. Probabilistic models have been also proposed for the reduction factors that reflects the influence of the eccentricity of the applied axial load and that of the debonding phenomenon on the axial capacity of the CFST columns. The probabilistic models for the axial capacity and the reductions factors are derived by means of a Bayesian approach taking into rational account, both, model parsimony and model accuracy. The predictive performance of the proposed probabilistic capacity models are discussed within a comparative assessment that involves existing formulations collected from some available technical standards and previous researches. To foster the use of the proposed formulation for design purposes, the paper also provides uncertainty factors calibrated to meet the reliability levels required by three different technical standards.

The novelty of the paper and the advantages of the proposed models are i) the moderate improvement of the accuracy level, ii) the probabilistic derivation that makes possible their easy implementation into fully probabilistic analyses, and iii) the possibility to update the models. Similarly to other capacity models calibrated on tests, the validity of the proposed models is restricted by the range of available experimental data. In this sense, the proposed probabilistic approach offers a significant advantage as compared to previous studies, because it enables the efficient models updating as new experimental data are available."

Acknowledgements

The work by Alessandro Contento and Giuseppe Quaranta is framed within the research project "Smart technologies and decision support tools for the assessment of deteriorating reinforced concrete infrastructures in seismic areas at territorial scale" (Grant No. RM120172B37F0628) funded by Sapienza Università di Roma. The authors gratefully acknowledge the financial support from the National Natural Science Foundation of China (Grant No. 51778148).

References

[1] M. Johansson and K. Gylltoft, "Structural behavior of slender circular steel-concrete composite columns under various means of load application," *Steel and Composite Structures*, vol. 1, no. 4, pp. 393–410, 2001.

[2] Y. Huang, B. Briseghella, T. Zordan, Q. Wu, and B. Chen, "Shaking table tests for the evaluation of the seismic performance of an innovative lightweight bridge with CFST composite truss girder and lattice pier," *Engineering Structures*, vol. 75, pp. 73–86, 2014.

[3] M.-G. Yang, C. S. Cai, and Y. Chen, "Creep Performance of Concrete-Filled Steel Tubular (CFST) Columns and Applications to a CFST Arch Bridge," *Steel and Composite Structures*, vol. 19, no. 1, p. 111–29, 2015.

[4] R. Yadav, B. Chen, H. Yuan, and Z. Lian, "Analytical Behavior of CFST Bridge Piers under Cyclic Loading," *Procedia Engineering*, vol. 173, pp. 1731–1738, 2017.

[5] D. Saini and B. Shafei, "Performance of Concrete-Filled Steel Tube Bridge Columns Subjected to Vehicle Collision," *Journal of Bridge Engineering*, vol. 24, no. 8, p. 04019074, 2019.

[6] K. Klöppel and W. Goder, "Traglastversuche mit ausbetonierten Stahlrohen und Aufstellung einer Bemessungsformel," *Der Stahlbau*, vol. 26, no. 1, pp. 1–10, 1957.

[7] C. D. Goode and D. Lam, "Concrete-Filled Steel Tube Columns-Tests Compared with Eurocode 4," in *Composite Construction in Steel and Concrete VI*, pp. 317–325, 2011.

[8] M. Denavit, "Steel-Concrete Composite Column Database," 2005.

[9] T. Zhong, B. Uy, L.-H. Han, and S.-H. He, "Design of concrete-filled steel tubular members according to the Australian Standard AS 5100 model and calibration," *Australian Journal of Structural Engineering*, vol. 8, no. 3, pp. 197–214, 2008.

[10] R. Leon, T. Perea, J. F. Hajjar, and M. Denavit, "Concrete-filled tubes columns and beam-columns: a database for the AISC 2005 and 2010 specifications," in *Festschrift Gerhard Hanswille*, vol. 20, pp. 203–212, 2011.

[11] J. Hajjar, B. Gourley, C. Tort, M. Denavit, P. Schiller, and N. L. Mundis, "Steel-concrete composite structural systems," 2013.

[12] J. Y. R. Liew, M.-X. Xiong, and D.-X. Xiong, "Design of concrete filled tubular beam-columns with high strength steel and concrete," *Structures*, vol. 8, pp. 213–226, 2016.

[13] S. Thai, H.-T. Thai, B. Uy, and T. Ngo, "Concrete-filled steel tubular columns: Test database, design and calibration," *Journal of Constructional Steel Research*, vol. 157, pp. 161–181, 2019.

[14] J. Y. R. Liew and M.-X. Xiong, *Design guide for concrete filled tubular members with high strength materials to Eurocode 4*. Research Publishing, 2015.

[15] H. G. Prion and J. Boehme, "Beam-column behaviour of steel tubes filled with high strength concrete," *Canadian Journal of Civil Engineering*, vol. 21, no. 2, pp. 207–218, 1994.

[16] D. Liu, W.-M. Gho, and J. Yuan, "Ultimate capacity of high-strength rectangular concrete-filled steel hollow section stub columns," *Journal of Constructional Steel Research*, vol. 59, no. 12, pp. 1499–1515, 2003.

[17] M. Mursi and B. Uy, "Strength of slender concrete filled high strength steel box columns," *Journal of Constructional Steel Research*, vol. 60, no. 12, pp. 1825–1848, 2004.

[18] D. Liu, "Tests on high-strength rectangular concrete-filled steel hollow section stub columns," *Journal of Constructional Steel Research*, vol. 61, no. 7, pp. 902–911, 2005.

[19] L.-H. Han, G.-H. Yao, and X.-L. Zhao, "Tests and calculations for hollow structural steel (HSS) stub columns filled with self-consolidating concrete (SCC)," *Journal of Constructional Steel Research*, vol. 61, no. 9, pp. 1241–1269, 2005.

[20] Q. Yu, Z. Tao, and Y.-X. Wu, "Experimental behaviour of high performance concrete-filled steel tubular columns," *Thin-Walled Structures*, vol. 46, no. 4, pp. 362–370, 2008.

[21] S.-H. Lee, B. Uy, S.-H. Kim, Y.-H. Choi, and S.-M. Choi, "Behavior of high-strength circular concrete-filled steel tubular (CFST) column under eccentric loading," *Journal of Constructional Steel Research*, vol. 67, no. 1, pp. 1–13, 2011.

[22] S. Guler, A. Çopur, and M. Aydogan, "Axial capacity and ductility of circular UHPC-filled steel tube columns," *Magazine of concrete research*, vol. 65, no. 15, pp. 898–905, 2013.

[23] F. Aslani, B. Uy, Z. Tao, and F. Mashiri, "Behaviour and design of composite columns incorporating compact high-strength steel plates," *Journal of Constructional Steel Research*, vol. 107, pp. 94–110, 2015.

[24] M.-X. Xiong, D.-X. Xiong, and J. Y. R. Liew, "Axial performance of short concrete filled steel tubes with high-and ultra-high-strength materials," *Engineering Structures*, vol. 136, pp. 494–510, 2017.

[25] S. Chen, R. Zhang, L.-J. Jia, J.-Y. Wang, and P. Gu, "Structural behavior of UHPC filled steel tube columns under axial loading," *Thin-walled structures*, vol. 130, pp. 550–563, 2018.

[26] M. Khan, B. Uy, Z. Tao, and F. Mashiri, "Behaviour and design of short high-strength steel welded box and concrete-filled tube (CFT) sections," *Engineering Structures*, vol. 147, pp. 458–472, 2017.

[27] A. H. Varma, J. M. Ricles, R. Sause, and L.-W. Lu, "Experimental behavior of high strength square concrete-filled steel tube beam-columns," *Journal of Structural Engineering*, vol. 128, no. 3, pp. 309–

318, 2002.

[28] A. H. Varma, J. M. Ricles, R. Sause, and L.-W. Lu, "Seismic behavior and design of high-strength square concrete-filled steel tube beam columns," *Journal of Structural Engineering*, vol. 130, no. 2, pp. 169–179, 2004.

[29] Z. Vrcelj and B. Uy, "Behaviour and design of steel square hollow sections filled with high strength concrete," *Australian Journal of Structural Engineering*, vol. 3, no. 3, pp. 153–170, 2002.

[30] J. Portolés, E. Serra, and M. L. Romero, "Influence of ultra-high strength infill in slender concrete-filled steel tubular columns," *Journal of Constructional Steel Research*, vol. 86, pp. 107–114, 2013.

[31] M.-X. Xiong, D.-X. Xiong, and J. Y. R. Liew, "Behaviour of steel tubular members infilled with ultra high strength concrete," *Journal of Constructional Steel Research*, vol. 138, pp. 168–183, 2017.

[32] M. L. Romero, C. Ibañez, A. Espinós, J. M. Portolés, and A. Hospitaler, "Influence of Ultra-high Strength Concrete on Circular Concrete-filled Dual Steel Columns," in *Structures*, vol. 9, pp. 13–20, Elsevier, 2017.

[33] M. Khan, B. Uy, Z. Tao, and F. Mashiri, "Concentrically loaded slender square hollow and composite columns incorporating high strength properties," *Engineering Structures*, vol. 131, pp. 69–89, 2017.

[34] D. Liu, "Behaviour of eccentrically loaded high-strength rectangular concrete-filled steel tubular columns," *Journal of Constructional Steel Research*, vol. 62, no. 8, pp. 839–846, 2006.

[35] S. Zhang and L. Guo, "Behaviour of High Strength Concrete-Filled Slender RHS Steel Tubes," *Advances in Structural Engineering*, vol. 10, no. 4, pp. 337–351, 2007.

[36] Y. Du, Z. Chen, Y.-B. Wang, and J. Y. R. Liew, "Ultimate resistance behavior of rectangular concrete-filled tubular beam-columns made of high-strength steel," *Journal of Constructional Steel Research*, vol. 133, pp. 418–433, 2017.

[37] W.-M. Gho and D. Liu, "Flexural behaviour of high-strength rectangular concrete-filled steel hollow sections," *Journal of Constructional Steel Research*, vol. 60, no. 11, pp. 1681–1696, 2004.

[38] M.-X. Xiong, D.-X. Xiong, and J. Y. R. Liew, "Flexural performance of concrete filled tubes with high tensile steel and ultra-high strength concrete," *Journal of Constructional Steel Research*, vol. 132, pp. 191–202, 2017.

[39] R. Zhang, S. Chen, P. Gu, and Y. Huang, "Structural behavior of UHPC filled steel tubular columns under eccentric loading," *Thin-Walled Structures*, vol. 156, p. 106959, 2020.

[40] J. Portolés, M. L. Romero, J. Bonet, and F. Filippou, "Experimental study of high strength concrete-filled circular tubular columns under eccentric loading," *Journal of Constructional Steel Research*, vol. 67, no. 4, pp. 623–633, 2011.

[41] H.-J. Lee, I.-R. Choi, and H.-G. Park, "Eccentric Compression Strength of Rectangular Concrete-Filled Tubular Columns Using High-Strength Steel Thin Plates," *Journal of Structural Engineering*, vol. 143, no. 5, p. 04016228, 2017.

[42] C. Ibañez, M. L. Romero, A. Espinós, J. M. Portolés, and V. Albero, "Ultra-high Strength Concrete on Eccentrically Loaded Slender Circular Concrete-filled Dual Steel Columns," in *Structures*, vol. 12, pp. 64–74, Elsevier, 2017.

[43] G. Li, B. Chen, Z. Yang, and Y. Feng, "Experimental and numerical behaviour of eccentrically loaded high strength concrete filled high strength square steel tube stub columns," *Thin-Walled Structures*, vol. 127, pp. 483–499, 2018.

[44] D. Hernández-Figueirido, M. L. Romero, J. Bonet, and J. Montalvá, "Ultimate capacity of rectangular concrete-filled steel tubular columns under unequal load eccentricities," *Journal of Constructional Steel Research*, vol. 68, no. 1, pp. 107–117, 2012.

[45] H.-S. Hu, K. Lin, B. M. Shahrooz, and Z.-X. Guo, "Revisiting the composite action in axially loaded circular CFST columns through direct measurement of load components," *Engineering Structures*, vol. 235, p. 112066, 2021.

[46] C. Ibañez, D. Hernández-Figueirido, and A. Piquer, "Effect of steel tube thickness on the behaviour of cfst columns: Experimental tests and design assessment," *Engineering Structures*, vol. 230, p. 111687, 2021.

[47] G. Giakoumelis and D. Lam, "Axial capacity of circular concrete-filled tube columns," *Journal of Constructional Steel Research*, vol. 60, no. 7, pp. 1049–1068, 2004.

[48] JTG/T D65-06-2015 (E), *Specifications for Design of Highway Concrete-Filled Steel Tubular Arch Bridges*. Ministry of Transport of the People's Republic of China, Beijing, China, 2015.

[49] GB 50923-2013, *Technical Code for Concrete-filled Steel Tube Arch Bridges*. Ministry of Housing and Urban-Rural Development of the People's Republic of China, Beijing, China, 2013.

[50] T.-T. Le, P. G. Asteris, and M. E. Lemonis, "Prediction of axial load capacity of rectangular concrete-filled steel tube columns using machine learning techniques," *Engineering with Computers*, pp. 1–34, 2021.

[51] M. Ahmadi, H. Naderpour, and A. Kheyroddin, "ANN Model for Predicting the Compressive Strength of Circular Steel-Confined Concrete," *International Journal of Civil Engineering*, vol. 15, no. 2, pp. 213–221, 2017.

[52] V.-L. Tran, D.-K. Thai, and D.-D. Nguyen, "Practical artificial neural network tool for predicting the axial compression capacity of circular concrete-filled steel tube columns with ultra-high-strength concrete," *Thin-Walled Structures*, vol. 151, p. 106720, 2020.

[53] M.-S. T. Nguyen, D.-K. Thai, and S.-E. Kim, "Predicting the axial compressive capacity of circular concrete filled steel tube columns using an artificial neural network," *Steel and Composite Structures*, vol. 35, no. 3, pp. 415–437, 2020.

[54] F. Lyu, X. Fan, F. Ding, and Z. Chen, "Prediction of the axial compressive strength of circular concrete-filled steel tube columns using sine cosine algorithm-support vector regression," *Composite Structures*, vol. 273, p. 114282, 2021.

[55] J. Moon, J. J. Kim, T.-H. Lee, and H.-E. Lee, "Prediction of axial load capacity of stub circular concrete-filled steel tube using fuzzy logic," *Journal of Constructional Steel Research*, vol. 101, pp. 184–191, 2014.

[56] Q. Ren, M. Li, M. Zhang, Y. Shen, and W. Si, "Prediction of ultimate axial capacity of square concrete-filled steel tubular short columns using a hybrid intelligent algorithm," *Applied Sciences*,

vol. 9, no. 14, p. 2802, 2019.

[57] H.-B. Ly, B. T. Pham, L. M. Le, T.-T. Le, V. M. Le, and P. G. Asteris, "Estimation of axial load-carrying capacity of concrete-filled steel tubes using surrogate models," *Neural Computing and Applications*, vol. 33, no. 8, pp. 3437–3458, 2021.

[58] P. Gardoni, A. Der Kiureghian, and K. Mosalam, "Probabilistic capacity models and fragility estimates for rc columns based on experimental observations," *ASCE Journal of Engineering Mechanics*, vol. 128, no. 10, pp. 1024–1038, 2002.

[59] I. Goodfellow, Y. Bengio, and A. Courville, *Deep Learning.* MIT Press, Cambridge, MA, 2016.

[60] J.-Q. Xue, A. Fiore, Z.-H. Liu, B. Briseghella, and G. C. Marano, "Prediction of ultimate load capacities of CFST columns with debonding by EPR," *Thin-Walled Structures*, vol. 164, p. 107912, 2021.

[61] M. D. O'Shea and R. Q. Bridge, "Design of circular thin-walled concrete filled steel tubes," *Journal of Structural Engineering*, vol. 126, no. 11, pp. 1295–1303, 2000.

[62] J. Zeghiche and K. Chaoui, "An experimental behaviour of concrete-filled steel tubular columns," *Journal of Constructional Steel Research*, vol. 61, no. 1, pp. 53–66, 2005.

[63] P. Gupta, S. Sarda, and M. Kumar, "Experimental and computational study of concrete filled steel tubular columns under axial loads," *Journal of Constructional Steel Research*, vol. 63, no. 2, pp. 182–193, 2007.

[64] N. J. Gardner and E. R. Jacobson, "Structural behavior of concrete filled steel tubes," in *Journal Proceedings*, vol. 64, pp. 404–413, 1967.

[65] F. E. Richart, A. Brandtzæg, and R. L. Brown, "A study of the failure of concrete under combined compressive stresses," tech. rep., University of Illinois at Urbana Champaign, College of Engineering, 1928.

[66] K. Susantha, H. Ge, and T. Usami, "A capacity prediction procedure for concrete-filled steel columns," *Journal of Earthquake Engineering*, vol. 5, no. 04, pp. 483–520, 2001.

[67] S. De Nardin, A. El Debs, *et al.*, "An experimental study of connections between i-beams and concrete filled steel tubular columns," *Steel and Composite Structures*, vol. 4, no. 4, p. 303, 2004.

[68] M. Johansson, "The efficiency of passive confinement in cft columns," *Steel and Composite Structures*, vol. 2, no. 5, pp. 379–396, 2002.

[69] K. Sakino, H. Nakahara, S. Morino, and I. Nishiyama, "Behavior of Centrally Loaded Concrete-Filled Steel-Tube Short Columns," *Journal of Structural Engineering*, vol. 130, no. 2, pp. 180–188, 2004.

[70] N. E. Shanmugam and B. Lakshmi, "State of the art report on steel–concrete composite columns," *Journal of Constructional Steel Research*, vol. 57, no. 10, pp. 1041–1080, 2001.

[71] J.-Q. Xue, B. Briseghella, and B.-C. Chen, "Effects of debonding on circular cfst stub columns," *Journal of Constructional Steel Research*, vol. 69, no. 1, pp. 64–76, 2012.

[72] S. Timoshenko, *History of strength of materials: with a brief account of the history of theory of elasticity and theory of structures.* Courier Corporation, 1983.

[73] S. Morino, "Concrete-filled steel tube column system: recent research and construction in Japan," in

Proceeding of the 1st Fib Congress, pp. 1–16, Japan, 2002.

[74] M. Hassanein, V. I. Patel, M. Elchalakani, and H.-T. Thai, "Finite element analysis of large diameter high strength octagonal cfst short columns," *Thin-Walled Structures*, vol. 123, pp. 467–482, 2018.

[75] F. E. Richart, A. Brandtzæg, and R. L. Brown, "Failure of plain and spirally reinforced concrete in compression," tech. rep., University of Illinois at Urbana Champaign, College of Engineering, 1929.

[76] M. Saatcioglu and S. R. Razvi, "Strength and ductility of confined concrete," *Journal of Structural engineering*, vol. 118, no. 6, pp. 1590–1607, 1992.

[77] AISC Committee and others, *Specification for structural steel buildings (ANSI/AISC 360-10)*. American Institute of Steel Construction, Chicago-Illinois, 2010.

[78] C. Goode and R. Narayanan, "Design of concrete filled steel tubes to ec4," in *Proceedings of the ASCCS Seminar on Concrete Filled Steel Tubes—A Comparison of International Codes and Practice*, pp. 1–25, Innsbruck, Austria, 1997.

[79] Eurocode 4, *Design of composite steel and concrete structures—Part 1.1: General rules and rules for buildings*. European Committee for Standardization, British Standards Institution, London, UK., 2004.

[80] F. Trentadue, G. Quaranta, and G. C. Marano, "Closed-form approximations of interaction diagrams for assessment and design of reinforced concrete columns and concrete-filled steel tubes with circular cross-section," *Engineering Structures*, vol. 127, pp. 594–601, 2016.

[81] F.-Y. Liao, L.-H. Han, and S.-H. He, "Behavior of cfst short column and beam with initial concrete imperfection: Experiments," *Journal of Constructional Steel Research*, vol. 67, no. 12, pp. 1922–1935, 2011.

[82] F.-Y. Liao, L.-H. Han, and Z. Tao, "Behaviour of cfst stub columns with initial concrete imperfection: analysis and calculations," *Thin-Walled Structures*, vol. 70, pp. 57–69, 2013.

[83] L.-H. Han, Y. Ye, and F.-Y. Liao, "Effects of core concrete initial imperfection on performance of eccentrically loaded cfst columns," *Journal of Structural Engineering*, vol. 142, no. 12, p. 04016132, 2016.

[84] S. Schnabl and I. Planinc, "Circumferential gap and partial debonding effects on buckling loads and modes of slender cfst circular columns," *Acta Mechanica*, vol. 230, no. 3, pp. 909–928, 2019.

[85] J.-Q. Xue, Y. Zhang, B. Briseghella, and B. Chen, "Experimental Research on Effects of Debonding on Circular CFST Columns with Different Slenderness Ratios," in *International Conference on Arch Bridges*, pp. 369–377, Springer, 2019.

[86] C. Guo and Z. Lu, "Air void and cap gap composite defects of concrete-filled steel-tube arch bridge transverse brace," *Journal of Performance of Constructed Facilities*, vol. 34, no. 4, p. 04020073, 2020.

[87] Y.-z. YE, Z.-h. WEN, and S.-w. PAN, "Experimental Research on Separation of Concrete-Filled Steel Tube and Effect of Pouring Pulp [J]," *Journal of Southwest Jiaotong University*, vol. 39, no. 3, pp. 381–385, 2004.

[88] J.-Q. Xue, B. Briseghella, and B.-C. Chen, "Parametric analysis of debonding on the circular CFST structures," in *Proceedings of the Structural Engineering World Congress (SEWC) 2011*, Como, Italy,

April 4–6, 2011.

[89] G. E. Box and G. C. Tiao, *Bayesian Inference in Statistical Analysis.* John Wiley & Sons, Ltd, 1992.

[90] C. J. Stone, *A course in probability and statistics*, vol. 19. Belmont: Duxbury Press, 1996.

[91] X. Wang, F. Fan, and J. Lai, "Strength behavior of circular concrete-filled steel tube stub columns under axial compression: A review," *Construction and Building Materials*, vol. 322, p. 126144, 2022.

[92] R Core Team, *R: A Language and Environment for Statistical Computing.* R Foundation for Statistical Computing, Vienna, Austria, 2020.

[93] ACI Committee 318, *Building Code Requirements for Structural Concrete: (ACI 318-95).* Farmington Hills, MI :American Concrete Institute, 1995.

[94] N. X. Ho and T.-T. Le, "Effects of variability in experimental database on machine-learning-based prediction of ultimate load of circular concrete-filled steel tubes," *Measurement*, vol. 176, p. 109198, 2021.

Appendix A. Existing models for the axial capacity of CFST columns

This appendix details the formulations used for the comparative assessment of the proposed probabilistic axial capacity models for CFST columns. Such formulations are divided between those retrieved from technical standards and those collected from the literature.

Appendix A.1. Formulations from technical standards

The axial capacity equation for CFST columns provided by EC4 [79] is one of the most detailed among the existing technical standards. It reads

$$N_u = \eta_a f_y A_s + \left(1 + \eta_c \frac{t}{D\frac{f_y}{f_c}}\right) A_c f_c, \tag{A.1}$$

where

$$\begin{cases} \eta_a = 0.25(3 + 2\bar{\lambda}) \\ \eta_c = 4.9 - 18.5\bar{\lambda} - 17\bar{\lambda}^2 \geq 0 \\ \bar{\lambda} = \frac{A_s f_y + A_c f_c}{\frac{\pi^2 (E_s I_s + 0.6 E_c I_c)}{L^2}} \\ E_c = 22000 \left(\frac{f_c+8}{10}\right)^{0.3} \end{cases}. \tag{A.2}$$

The predictions obtained with this formulation are valid for 20MPa $\leq f_c \leq$ 60 MPa, $f_y \leq$ 460 MPa, and $D/t \leq 0.15 E_s/f_y$.

The capacity equations reported into AISC [77] and ACI [93] are comparatively simpler than the one in EC4. Specifically, the capacity equation for N_u adopted by AISC is the following:

$$N_u = A_s f_y + 0.95 A_c f_c, \tag{A.3}$$

and its use is limited to 21 MPa $\leq f_c \leq$ 70 MPa, $f_y \leq$ 525 MPa, $A_s \geq 0.01 A_g$ (where A_g is the gross area of the cross-section), and $D/t \leq \sqrt{8E_s/f_y}$.

The capacity equation reported by ACI reads

$$N_u = A_s f_y + 0.85 A_c f_c. \tag{A.4}$$

Lastly, the capacity equation given by GB50923-2013 is the following:

$$N_u = \phi \phi_e k_3 (1.14 + 1.02\xi)(1 + \rho_c) f_c A_c \tag{A.5}$$

where k_3 is the conversion coefficient of design axial compressive strength defined in [49], and $\rho_c = A_s/A_c$ is the steel ratio of CFST column cross-section. The two coefficients ϕ_e and ϕ are the reduction factor for the load eccentricity and the stability coefficient, respectively. They depend on the load eccentricity e, the cross-sectional radius of the concrete core r_c, and the relative slenderness ratio λ_n as follows:

$$\phi_e = \begin{cases} \frac{1}{1+1.85\frac{e}{r_c}}, & \frac{e}{r_c} \leq 1.55 \\ \frac{1}{2.50\frac{e}{r_c}}, & \frac{e}{r_c} > 1.55 \end{cases}, \tag{A.6}$$

$$\phi = \begin{cases} 0.658^{\lambda_n^2}, & \lambda_n \leq 1.5 \\ \frac{0.877}{\lambda_n^2}, & \lambda_n > 1.5 \end{cases}, \tag{A.7}$$

with

$$\lambda_n = \frac{\lambda_0}{\pi} \sqrt{\frac{f_y A_s + f_c A_c + A_c \sqrt{\rho_c f_y f_c}}{E_s A_s + E_c A_c}}, \tag{A.8}$$

where $\lambda_0 = 4L/D$, which is the nominal slenderness ratio. The predictions obtained with this formulation are valid for 20.1 MPa $\leq f_c \leq$ 38.5 MPa, 235 MPa $\leq f_y \leq$ 390 MPa, $35(235/f_y) \leq D/t \leq 100(235/f_y)$, $0.04 \leq \rho_c \leq 0.20$, and $\xi \geq 0.60$.

Appendix A.2. Formulations from literature

The formulations used for the comparative assessment collected from the literature are presented in chronological order. The capacity equation by Goode and Narayanan [78] is the following:

$$N_u = \frac{6t}{D-2t} A_s f_y + 0.85 A_c f_c. \tag{A.9}$$

The formulation proposed by Giakoumelis and Lam [47] reads

$$N_u = A_s f_y + 1.3 A_c f_c. \tag{A.10}$$

Ho and Le [94] used different methods to estimate the axial capacity of CFST columns. Among the final formulations, the one carried out via support vector machine has been considered in the present study. Such a capacity equation can be written in matrix form as follows:

$$N_u = \boldsymbol{\alpha} \left[\left(\boldsymbol{I} + \frac{\boldsymbol{\beta}}{\omega^2} \boldsymbol{X} \right)^3 \right] + b \tag{A.11}$$

where $\boldsymbol{\alpha}$ is the difference between two Lagrange multipliers of the support vectors, $\boldsymbol{I}$ is the identity matrix, $\boldsymbol{\beta}$ is the support vector matrix, $\boldsymbol{X}$ is the standardized input vector matrix, ω is the kernel scale parameter, b is a scalar bias parameter. The interested reader is referred to [94] for more details.